Finanziato dall'Unione europea NextGenerationEU
Ministero dell'Università e della Ricerca
Italiadomani PIANO NAZIONALE DI RIPRESA E RESILIENZA

multi-Risk sciEnce for resilienT commUnities undeR a changiNgclimate

Codice progetto MUR: **PE00000005** – CUP LEAD PARTNER: **F83C22001660002**

Integrated multi-risk urban impact assessment and forecasting at variable scale

DV 5.3.4

Finanziato dall'Unione europea NextGenerationEU | Ministero dell'Università e della Ricerca | Italiadomani PIANO NAZIONALE DI RIPRESA E RESILIENZA

RESEARCH GROUP

Pier Lugi Bragato (Leader T5.3.4), Antonella Peresan, Hany M. Hassan Elsayed, Hazem Badreldin, Chiara Scaini, Elisa Zuccolo ***(OGS)***; Francesca Borghi, Erika Brattich, Francesco Decataldo, Andrea Faggi, Francesca Ferretti, Tiziano Maestri, Eva Vanna Lorenza Negri, Luca Pozza (Leader WP 5.3) ***(University of Bologna);*** Maria Grazia Badas, Gianluca Gatto, Amit Kumar, Sabrina Lai, Federica Leone, Santhosh Paramasivam, Giorgio Querzoli, Corrado Zoppi ***(University of Cagliari);*** Chiara Arrighi, Gianni Bartoli, Simona Francalanci, Federico Gusella, Rocco Novellino, Barbara Pintucchi, Marco Uzielli, Paola Vannucchi ***(University of Florence)***; Giovanni Besio, Rosella Bovolenta, Federico Canepa, Serena Cattari, Arianna Cauteruccio, Francesco De Leo, Sergio Lagomarsino, Andrea Lira Loarca, Dario Massabò, Federico Mazzei, Luisa Pagnini, Giuseppe Piccardo, Margherita Rago, Paola Salmona ***(University of Genoa)***; Roberto Castelluccio, Maria Fabrizia Clemente, Valeria D'Ambrosio, Carlo Del Gaudio, Federica dell'Acqua, Mariano Di Domenico, Ferdinando Di Martino, Mariacarla Fraiese, Rossella Marmo, Vittorio Miraglia, Maria Polese, Chiara Russo, Antonio Sferratore, Gabriella Tocchi, Gerardo Verderame, Cristina Visconti, Veronica Vitiello ***(University of Naples Federico II);*** Annamaria Belleri, Roberto Lollini, Massimiliano Pittore, Stefan Schneiderbauer, Daniele Vettorato, Gioberti Morantes ***(EURAC).***

Contributors

Luca Pozza (Leader WP 5.3), Pier Luigi Bragato (Leader T5.3.4)

Conceptualization, Methodology, Formal analysis, Data curation, Review

Pier Lugi Bragato, Antonella Peresan, Hany M. Hassan Elsayed,
Hazem Badreldin, Chiara Scaini, Elisa Zuccolo *(OGS)*

1. Introduction; 2. Towards operative impact assessment and forecasting for multiple hazards; 3.1 High-resolution multi-hazard residential buildings and population exposure model for coastal areas: a case study in northeastern Italy

Roberto Castelluccio, Rossella Marmo,
Veronica Vitiello, Mariacarla Fraiese *(University of Naples Federico II)*

3.2 Identifying the risks arising from the building envelope vulnerability to several hazards

Dario Massabò, Federico Mazzei *(University of Genoa)*

3.3 Monitoring and impact forecasting models for air pollution; 3.4 Integrated assessment of health-connected risks from air pollution with a special focus on emerging pollutants

Rocco Novellino, Paola Vannucchi *(University of Florence)*

3.5 A detailed 3D geological model of the Florence basin for the estimation earthquake scenarios

1. Technical References

Project Acronym	RETURN
Project Title	multi-Risk sciEnce for resilienT commUnities undeR a changiNg climate
Project Coordinator	Domenico Calcaterra UNIVERSITA DEGLI STUDI DI NAPOLI FEDERICO II domcalca@unina.it
Project Duration	December 2022 – November 2025 (36 months)

Deliverable No.	DV 5.3.4
Dissemination level*	PU
Work Package	WP3 – Multi-risk vulnerability and impact assessment and forecasting
Task	T 5.3.4 - Integrated multi-risk urban impact assessment and forecasting at variable scale
Lead beneficiary	OGS
Contributing beneficiary/ies	OGS, UNIFI, UNIGE, UNINA

* PU = Public

PP = Restricted to other program participants (including the Commission Services)

RE = Restricted to a group specified by the consortium (including the Commission Services)

CO = Confidential, only for members of the consortium (including the Commission Services)

2. Technical References

Version	Date	Lead contributor	Description
1.0	16/06/2025	OGS	First release

Summary

List of Figures

List of Tables

1. Introduction

The present **Deliverable 5.3.4** *"Integrated multi-risk urban impact assessment and forecasting at variable scale"* summarizes the results of the work of four research groups from OGS (Istituto Nazionale di Oceanografia e di Geofisica Sperimentale), UNIFI (University of Florence), UNIGE (University of Genoa) and UNINA (University of Naples Federico II) related to the **Task 5.3.4** (same title as the Deliverable) of the **Work Package WP 5.3** "*Multi-risk vulnerability and impact assessment and forecasting*" within **Spoke 5 TS1** "*Urban and metropolitan settlements*" of the **RETURN** project. It takes advantage of the other WPs and Tasks of **Spoke 5 TS1**, which define a unified framework for different disciplines with different approaches to characterize and quantify hazards, exposure and vulnerability. Here the focus is on the impact of the events, either measured or predicted, to take actions that can support the rescue organization (after an event) or mitigate their effect in the long term through urban planning.

The topic of impact assessment and forecasting is quite broad, so we were forced to adopt a specific approach based on the attitudes and areas of expertise of the research groups involved. In particular, the document is divided into two main parts. The first part (**Chapter 2** *"Towards operational impact assessment and forecasting for multiple hazards"*) follows the experience of the OGS in collaboration with the regional civil protections of Friuli Venezia Giulia and Veneto and aims at developing and tuning procedures that support emergency management related to various geohazards in urban settlements (earthquakes, landslides and tsunamis). Impact assessment here is mainly done using innovative sensor networks, while impact prediction is meant in a rather limited (but still useful) sense: anticipating the potential impact of an event shortly after it occurs, but in time to take action to mitigate the impact. The second part (**Chapter 3** "*Knowledge bases for improving impact assessment and forecasting*") does not refer to operational procedures. Rather, it gathers data, tools, methods and perspectives from the literature review that are useful for future developments to implement systems with improved capacity for impact assessment and forecasting. The chapter is organized into five independent sections, devoted respectively to the development of a high-resolution and multi-hazard exposure model for residential buildings and population (**Section 3.1**); the assessment of the risks posed by the building envelope exposed to various hazards (**Section 3.2**); the development of models to predict the impact of air pollution (**Section 3.3**) and its effects on human health (**Section 3.4**). The last contribution (**Section 3.5**) concerns the creation of a very detailed geological model useful for assessing the potential impact of earthquakes in a particular urban environment such as the city of Florence.

Note : This document is to be intended as part of an ongoing iterative process. As such it will be subject to further updates and modifications in the following phases of the project, also according to the feedback and consultations among the project partners and with the stakeholders.

2. Towards operational impact assessment and forecasting for multiple hazards

This chapter illustrates procedures developed by the OGS to rapidly assess the effects of a natural disaster or to predict its possible consequences immediately after its occurrence in order to take timely protective measures and mitigate the consequences. Following the approach of the **RETURN** project and in particular of the **Task 5.3.4**, the overall system considers multiple hazards (specifically, three geohazards: earthquakes, landslides and tsunamis) with impacts at a variable spatial scale ranging from the individual building to the municipal and regional level. The common focus is on rapid assessment with automatic or semi-automatic procedures to support civil protection for emergency management. Some of the solutions described here are currently being used as part of cooperation agreements with the regional civil protections of Friuli Venezia Giulia and Veneto, while others are still at the prototype stage.

According to the operational approach outlined here, the hazardous events (earthquakes, landslides and tsunamis) are considered individually after their occurrence. However, according to the classification of multi-hazard relationships outlined in **Deliverable 5.2.1** "*Risk-Oriented Taxonomy and Ontology of Urban Subsystems and Functional Models*", they have a triggering relationship with each other and with other triggering hazards. Quite simply, tsunamis are triggered by earthquakes, while landslides can be triggered by earthquakes and extreme meteorological conditions (e.g. heavy rainfall).

2.1 Rapid impact assessment

The rapid impact assessment is carried out for earthquakes and landslides. In both cases it exploits high-density networks based on cost-effective instruments, namely an accelerometer network in Veneto (Bragato et al., 2025, to be extended to Friuli Venezia Giulia) and a network of single-frequency GPS stations (Zuliani et al., 2022; Tunini et al., 2024).

2.1.1 Dense accelerometer monitoring of earthquakes

Earthquake monitoring in urban settlements is carried out using a network of 320 MEMS accelerometers covering more than 50% of the municipalities in Veneto (Fig. 1). They are installed at the base of structures representative of the residential building stock (mainly reinforced masonry buildings), owned by public institutions (mostly municipalities) and two private companies: FiberCop s.p.a., hosting sensors in 120 telephone exchange buildings, and Poste Italiane s.p.a., hosting accelerometers in 42 post offices (Fig. 2). Twenty-two buildings are additionally equipped with a sensor near the roof to experiment techniques for rapid damage assessment of individual buildings based on the inter-story drift ratio.

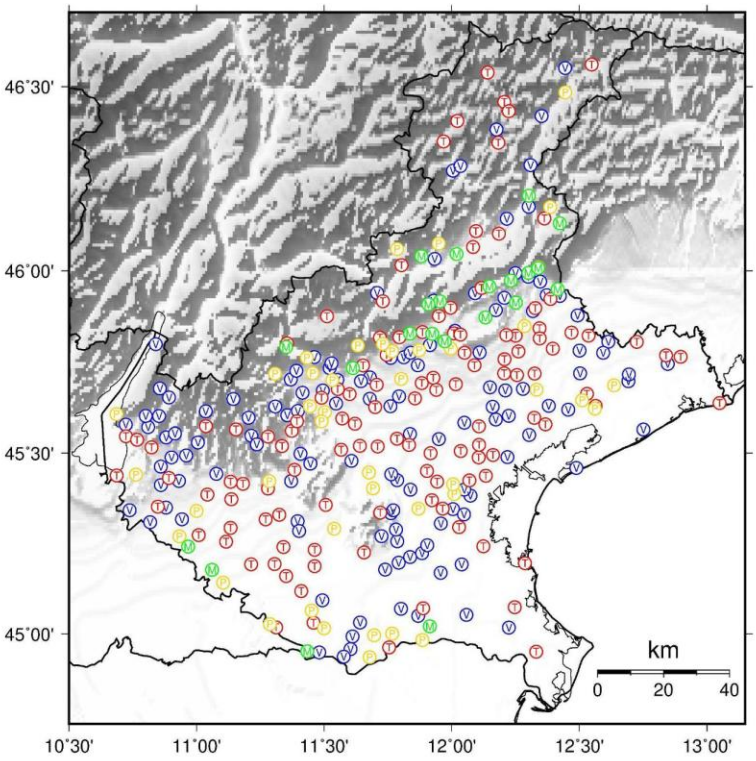

Figure 1 Dense accelerometer network in Veneto: civil protection volunteer organizations (V); FiberCop s.p.a. telephone exchanges (T); Poste Italiane s.p.a. post offices (P); municipalities and other public buildings (M).

Figure 2 Accelerometers installed at the top and at the bottom of a public building.

After an earthquake, the recorded data are used to obtain:

- direct shaking measures at the monitored building (Fig. 3);
- shaking estimations at the municipal and regional level (Fig. 4), where shaking data are interpolated using the ShakeMap software (Worden et al., 2020);
- damage estimation for the monitored buildings:
    a) from engineering-estimated PGA thresholds (from "Schede di verifica sismica di edifici strategici o rilevanti", only a few available);
    b) using recordings at the bottom and simplified dynamic modelling (DARR method, Petrovic et al., 2023);
- damage estimation for municipalities (number of buildings in the damage classes D4-D5, Fig. 5) based on shaking, fragility curves and exposure from ISTAT census data (RDSA system, Poggi et al., 2021).

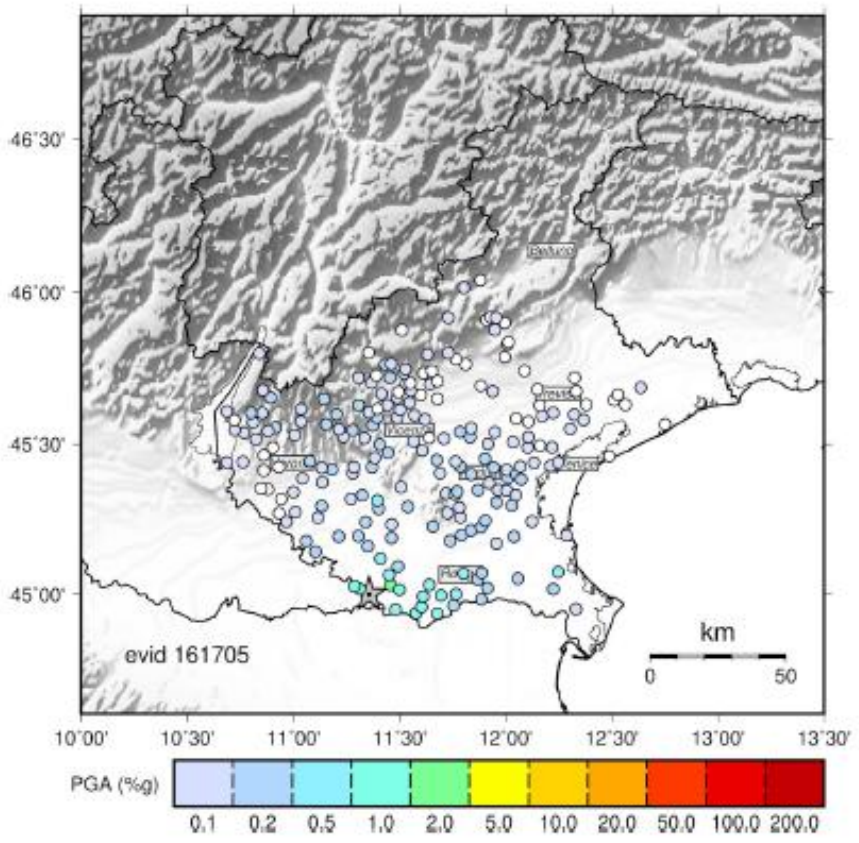

Figure 3 Shaking measures at the basement of the monitored buildings for a magnitude ML 4.3 earthquake.

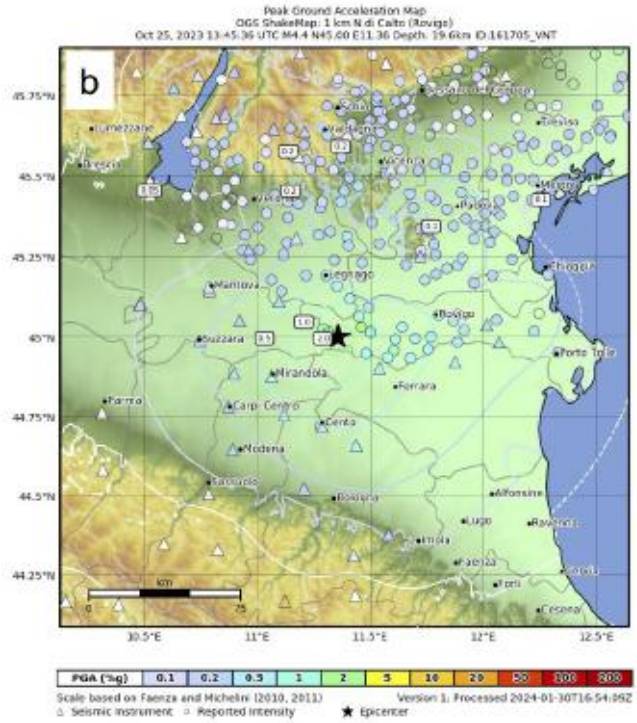

Figure 4 Shaking estimated at the regional level for a magnitude ML 4.3 earthquake.

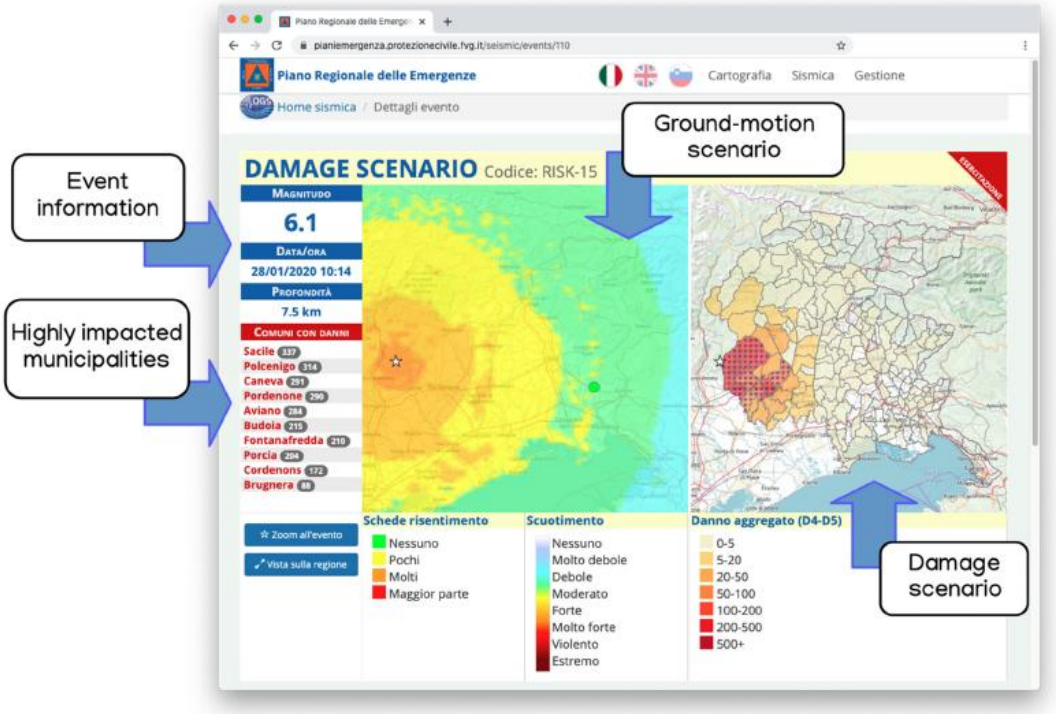

Figure 5 Example of damage estimation at the municipality level (number of buildings in the damage classes D4 and D5) for a hypothetical magnitude 6.1 earthquake.

2.1.2 Landslide monitoring for alert purposes

A dense network of 12 cost-effective single-frequency GPS stations is currently deployed to monitor the movements of a landslide threatening the village of Cazzaso in the Carnic Alps (northeaster Italy, Fig. 6). The network is completed by one permanent, high-quality, dual-frequency GNSS station located in a stable area by the village. Its main objective is to assess the impact of heavy rain episodes that accelerates the landslide (blue vs. black lines in Fig. 7). The details of the implementation as well as the motivations that led to prefer this solution to other alternatives are described with details by (Zuliani et al., 2022).

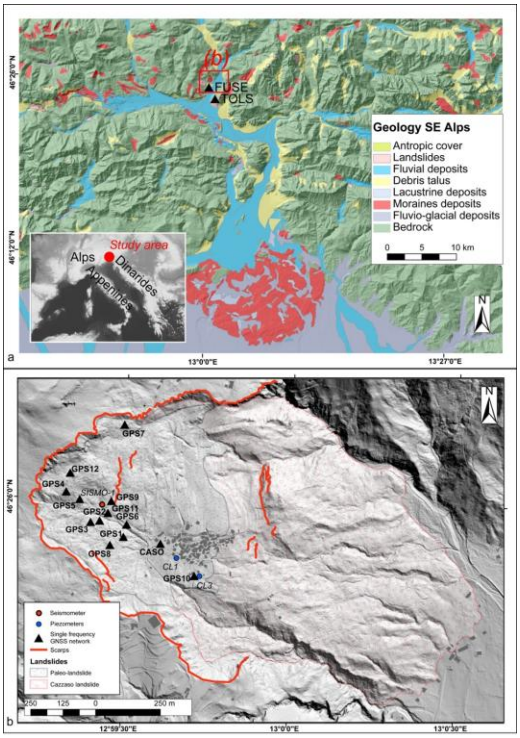

Figure 6 Dense network of 12 single-frequency GPS stations monitoring a landslide in the village of Cazzaso in northeastern Italy (GPS1-GPS12, CASO is the standard, high-quality dual-frequency GNSS station located in the village).

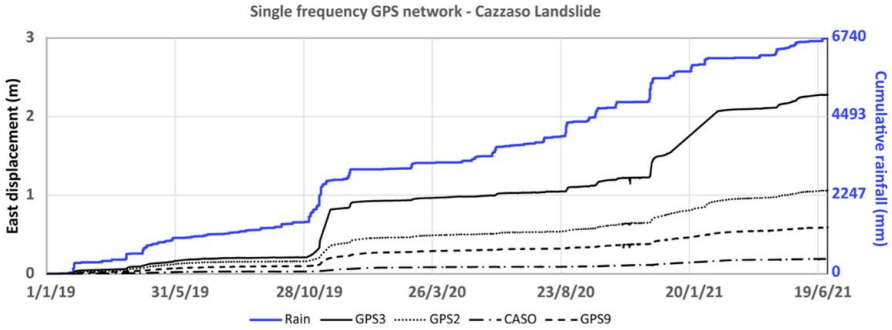

Figure 7 Displacement toward the East recorded by the cost-effective, single-frequency GPS network on the Cazzaso landslide between 1 January 2019 and 30 June 2021. The black lines with different patterns indicate the different stations (CASO is the standard, high-quality dual-frequency GNSS station located in the village of Cazzaso). The blue line indicates the cumulative measurement of rainfall recorded by the Tolmezzo rainfall gauge.

2.2 Rapid impact forecasting for impact mitigation

The impact forecasting methods used by OGS are not aimed at predicting the hazardous event. Rather, the aim is to anticipate possible consequences after the event in order to enable a useful response. The types of events, the basic prediction mechanism and the time allowed for the response are described below:

- earthquakes: early warning exploiting S-P delay (within seconds);
- landslides: alerting based on observed movements (from minutes to days);
- tsunami: alerting based on earthquake information (from tens of minutes to hours in northeastern Italy, depending on the distance from the source).

The solution implemented for landslide warning works with the data from the GPS monitoring described above. An automatic warning system, managed in collaboration between OGS, the Municipality of Cazzaso and the Regional Civil Protection and Geological Service of Friuli Venezia Giulia, issues three warning levels (yellow, orange and red) for increasing landslide velocity values. Actions are assigned to each alert level in the municipality's civil protection plan.

The solutions for earthquakes and tsunamis are still under development at the level of a prototype (for earthquakes) or preliminary studies (for tsunamis), described in more detail in the following.

2.2.1 Earthquake early warning

The earthquake early warning system under implementation should operate at a local level, exploiting data and processing capabilities of each accelerometer of the dense seismic network described above. It uses the characteristics of the P-waves to predict the intensity of the horizontal shaking produced by the following S-waves, leaving a few seconds for a response. The estimation can be done according to different methods published in the literature. Fig. 8 illustrates the method of (Caruso et al., 2017): based on the vertical peak ground displacement of the P-waves (Pd in Fig. 8b), it predicts the horizontal peak ground velocity (PGV in Fig. 8a) and, based on an empirical relationship, the macroseismic intensity at the site. The estimation is repeated with increasing confidence (although leaving less time for response) using 1, 2 or 3 seconds of the vertical signal. Pre-alerting time increases with distance from the hypocenter (e.g. about 4 seconds for a site 40 km from the hypocenter). The very short time should allow for basic human self-protection measures and automatic shutdown of equipment and facilities.

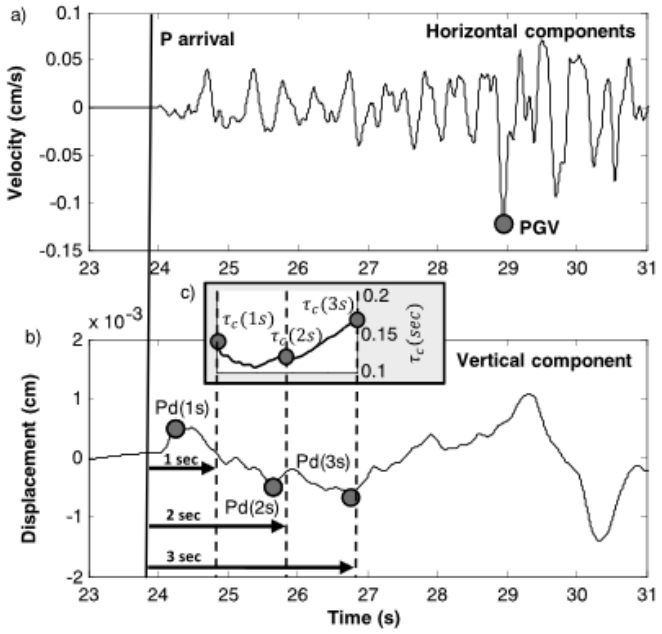

Figure 8 Features of the seismograms considered by the earthquake early warning system by Caruso et al. (2017)

2.2.2 Modelling of earthquake-induced tsunami hazard scenarios: a case study in Northern Adriatic

Physical modelling of earthquakes and cascading hazards, such as tsunamis or landslides, provides the basis for defining impacts and multi-risk scenarios. Significant earthquake-induced tsunamis in the Northern Adriatic are rare, with most historical events reported along the central and southern coasts, hence related risk awareness is limited. Although a tsunami alert system has been established for the Mediterranean region and connected seas, a detailed understanding of the potential impacts of tsunami waves on coastal areas is still lacking for many sites. Here we consider hazard scenarios associated with potential tsunamis generated by offshore earthquakes to contribute to tsunami risk assessments for urban areas along the Northeastern Adriatic coasts (e.g. Peresan and Hassan, 2024). Tsunami modelling is conducted using the NAMI DANCE software (e.g. Yalciner et al., 2006 and references therein), which accounts for seismic source properties, bathymetry, topography and non-linear effects in wave propagation. Earthquake induced hazard scenarios are developed for selected coastal areas of Northeastern Italy, focusing on selected cities such as Trieste and Lignano. The modelling considers a wide set of potential earthquake-induced tsunami scenarios, with sources defined based on historical tsunami catalogues and active fault databases. Existing bathymetry and topography datasets are refined to incorporate high-resolution data, and to better capture small-scale coastal features that influence tsunami inundation. The modelling provides a set of tsunami hazard-related parameters, such as inundation maps, which are relevant for characterising tsunami impacts in these areas.

For effective multi-hazard disaster risk reduction and mitigation, high-resolution exposure models are needed at the local scale, especially for hazards like tsunamis, which exhibit high spatial variability. We may consider the methodology for developing high-resolution exposure models for population and

residential buildings (described in Section 3.1) to support impact and multi-hazard risk assessments. Building census data is enhanced with exposure indicators, such as built area, replacement cost, height, and plan regularity, derived from digital building footprints. These high-resolution exposure models, integrated with tsunami hazard maps, allow improving the resolution of impact and damage assessments.

2.2.2.1 Modelling of earthquake-induced tsunami hazard scenarios: a case study in Northern Adriatic

The National Alert System for earthquake generated tsunamis (SiAM - Sistema Allertamento Maremoti) has been established in 2017 (Directive of the President of the Council of Ministers, 17 February 2017). Within this formal framework, the CAT-INGV (Centro Allerta Tsunami, managed by INGV) operates at the Italian national level, with the aim of disseminating alert messages to the territory, including local authorities. Since 2017, various tsunamis have been assigned a "watch" alert level (i.e. red alert, with an offshore wave amplitude estimate >50 cm, and a run-up >1 m) by the CAT-INGV system, (e.g. 2nd May 2020, Crete; 30th October 2020, Aegean Sea; 6th February 2023, Turkey). Detailed tsunami inundation maps, however, are not yet available for the Northeast Adriatic coasts between Trieste and Lignano. The available tsunami probabilistic hazard estimates (e.g. NEAMTHM18 maps, Basili et al., 2019), in fact, are provided for sites located along the 50m depth isobaths. In the Northern Adriatic and similar coasts, where the bathymetry is extremely shallow (well below 50 meters), the distance between these isobaths and the coastline is very large, and the use of empirical relationship may well turn out inadequate. In addition, in the alert messages, an upper bound is not provided for the tsunami wave amplitude (or a run-up) in the area of interest. According to the mentioned SiAM directive, the accuracy and reliability of inundation data derived from existing probabilistic tsunami hazard estimates, can be improved by carrying out detailed investigations at local scale (e.g., municipal level and port areas), integrating its results with detailed studies through physical-numerical modelling. This is especially important for urban areas, which are characterised by high exposure and population density.

To assess tsunami hazard for the urban cities located along the northeast Adriatic coastal zone, a wide set of tsunami scenarios has been computed, considering the possible tsunamigenic sources as defined in the most updated database of seismogenic sources. Parametric tests have been performed as well, to account for seismic source variability and a localized high-resolution Digital Terrain Model (DTM), has been used as topographic and bathymetry dataset for the tsunami simulations. Specifically, these studies have been accomplished accounting for the recently updated DISS database of seismogenic sources in the Adriatic Sea, and considering different potential tsunamigenic sources of tectonic origin, located in three distance ranges from the areas of interest (namely at Adriatic-wide, regional and local scales). A nested grid of different resolution domains of topographic-bathymetric data was adopted from open access and local sources; the large domain, with coarse bathymetry is taken from GEBCO-2020, while the smaller domain is taken from EMODnet.

According to the study by Peresan and Hassan (2024) physically consistent tsunami hazard estimates can be obtained based on the modelling of tsunami waves propagation from a wide set of possible sources. The possible tsunamigenic earthquake sources located within the Adriatic Sea have been considered, defined based on the updated DISS database (DISS-3.3 http://diss.rm.ingv.it/diss/) and considering the constraints, in space and magnitude domains, of the tsunami decision matrix adopted by CAT-INGV. According to the decision matrix, a seismogenic source is considered tsunamigenic, of potential weak

local tsunami (distance ≤ 100 km), if it can produce shallow offshore earthquakes of magnitude M≥6. Therefore, a database of local tsunamigenic earthquake sources of Mmax≥6 relative to our area of interest (i.e. the coastal area between Lignano and Trieste) and Mmax≥6.5 for regional (100 km < distance ≤ 400) and basin-wide (distance > 400 km) tsunamis, has been extracted from the DISS-3.3 database.

The compilation of the related database of tsunami scenarios allows us to evaluate the potential tsunami hazard at different distances and might serve as pre-computed scenarios in case a possible tsunami alert. In case of tsunamigenic earthquake occurrence, the results for best matched pre-computed scenario (in location and magnitude) can be extracted. Remarkably, the maximum magnitude of most seismogenic sources within the DISS-3.3 was upgraded, with a general increase relative to the previous DISS-3.2.1 version; this should be regarded as a warning about the uncertainty on the magnitude of future events. Further specific studies have been carried out recently for possible tsunamigenic earthquakes in Southern Adriatic, with a focus on the Montenegro-Albania source zones, and aimed at the assessment of expected inundation (Xhafaj et al., 2024) in Durres and other coastal municipalities in Albania. Tsunamigenic earthquake sources, associated with large events (M>7.5) in Southeastern Adriatic may have a significant impact also on Italian coasts (e.g. Apulia).

2.2.2.2 The 9th November 2022 Pesaro earthquake

A strong shallow earthquake of magnitude Mw5.7 (Modified Mercalli Intensity Scale-MMI~VI) struck Italy's Adriatic coast on the 9th November 2022 (Fig. 9), without causing serious damage or injuries. Its epicentre was located about 35 km offshore from Pesaro, a seaside city in the eastern Marche region, at a depth of 7 km. More than 450 aftershocks of magnitude between 2 and 4.6 were recorded after this earthquake and till end the 31th January 2023. Plotting the main event and aftershock distribution shows that they overlap with the ITCS106-Pesaro mare-Cornelia source characterized by a maximum magnitude-Mmax of 6.5 according to DISS-3.3.0 (Fig. 10). The occurrence of this offshore earthquake raised the concern regarding the potential of tsunami generation by larger magnitude event or worst-case scenario and their impacts on the coasts in vicinity and north the Adriatic which they have a great socio-economic value. This motivated the simulation of tsunami hazard scenarios for the strongest earthquakes associated with this seismogenic source.

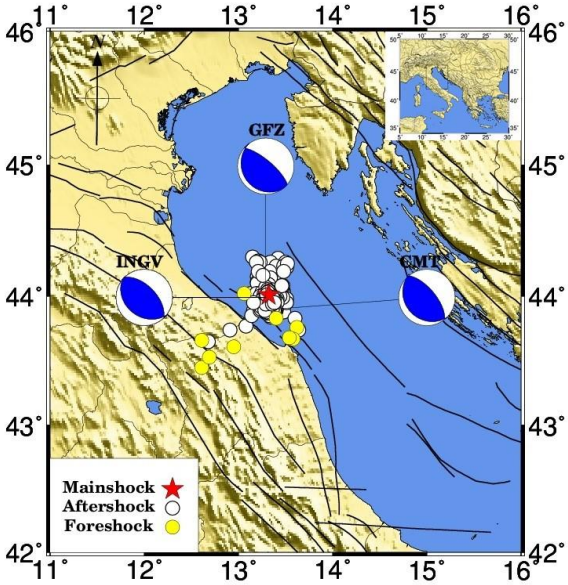

Figure 9. The 9th November 2022 earthquake swarm and moment tensor solutions computed by INGV, GCMT, and GFZ agencies for the Mw5.7 main event. Yellow circle marks represent foreshocks, red star refer to the mainshock, while white circle are aftershocks (after EMSC catalogue).

2.2.2.3 Tsunami hazard scenario for ITCS106 seismogenic source

The potential tsunami hazard was assessed for the seismogenic zone, where the 09th November main shock and its swarm occurred, based on the maximum earthquake magnitude provided for the ITCS106 source in the DISS-3.3.0 database, specifically the Pesaro mare-Cornelia seismogenic source of Mmax=6.5 (http://diss.rm.ingv.it/diss/ as last access Feb 2023). The fault length, width and slip are estimated from existing source scaling relationship (Wells & Coppersmith, 1994). Based on parametric studies for each scenario the parameters that compose the worst-case scenarios in terms of strike, dip, rake and focal depth were extracted from the given range in the DISS-3.3.0 database and used for the simulations. Since the fault dimension obtained by the empirical magnitude scaling relationship, we allowed modelled scenarios to float in order to model all possible scenarios and finally we compute an aggregated scenario that accounts for such variability.

Tsunami modelling was performed by NAMI DANCE code (Yalciner et al., 2006), which allows accounting for seismic source properties, nested bathymetry grids, and non-linear effects in wave propagation and inundation. Two domains topo-bathymetry grids were considered. A coarse-domain bathymetry grid of 400 m spatial resolution for the Adriatic Sea was extracted from GEBCO-2020. Also, medium-domain of 111 m resolution grid was obtained and processed from the EMODnet portal (https://portal.emodnet-bathymetry.eu/) for both regions of interest.

A number of tsunami hazard scenarios that reflect the variation in location and source parameter within the ITCS106 source were computed, and maximum wave height in meter and travel time at selected points of interest were extracted. The computed maximum wave height for the nearest coast of Pesaro is about 1.1 m and estimated time of arrivals is 20 minute (Fig. 10 and Table 1).

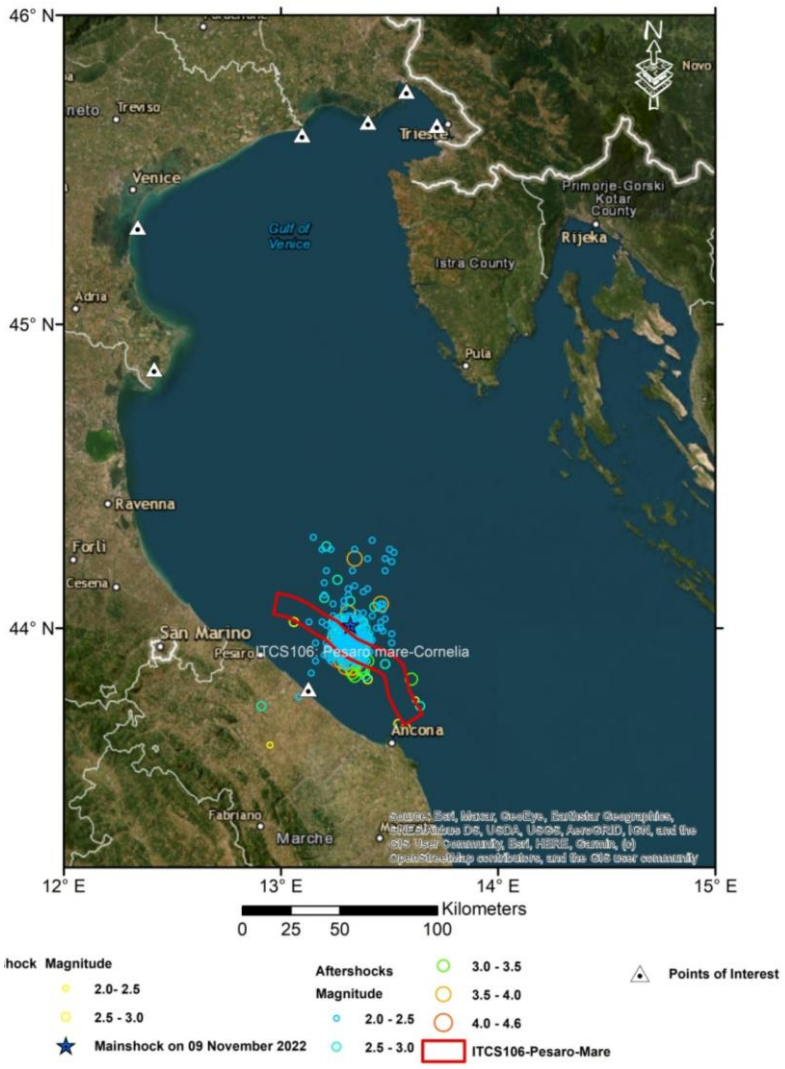

Figure 10. ITCS106 Seismogenic source Mw6.5 (Red Rectangle) along with observed seismicity related to 2022 Pesaro earthquake. The points of interest (POI), at which tsunami maximum wave height and travel time of tsunami waves are computed, are marked by white triangles (Table 1).

Table 1. The computed maximum wave height (Hmax) and tsunami travel time (TT) at the selected points of interest (POI) in Figure 10.

Latitude	Longitude	Hmax (m)	TT min	Location
43.7983	13.1267	1.1	20	Pesaro
44.2455	13.3737	0.25	40	Rimini
45.3173	12.3412	0.2	146	Venice
45.6155	13.0982	0.2	180	Lignano
45.6571	13.4018	0.2	183	Grado
45.7566	13.5788	0.2	185	Monfalcone
45.6464	13.7188	0.2	187	Trieste
44.8545	12.4171	0.2	105	Po Delta

3. Knowledge bases for improving impact assessment and forecasting

3.1 High-resolution multi-hazard residential buildings and population exposure model for coastal areas: a case study in northeastern Italy

Multi-hazard disaster risk analysis, including impact assessment and forecasting, requires combining exposure information developed at different spatial resolutions and scales (i.e. global, regional, national, local). The spatial resolution of exposure data, which is often aggregated at a broader scale and lower resolution, may not be comparable with the spatial variability and extent of certain hazards affecting coastal areas (e.g. tsunamis, floods, landslides, and coastal erosion). Traditionally, efforts in the field were focused on assessing exposure independently for different hazardous phenomena, depending on their spatial scales (e.g. floods, Figueiredo and Martina, 2016; earthquakes, Tocchi et al., 2022). In this work, we propose and introduce a methodology to develop high-resolution exposure assessment of urban areas, to be used for multi-hazard risk reduction purposes at a city or municipality scale, combining global, national and local datasets (Fig. 11).

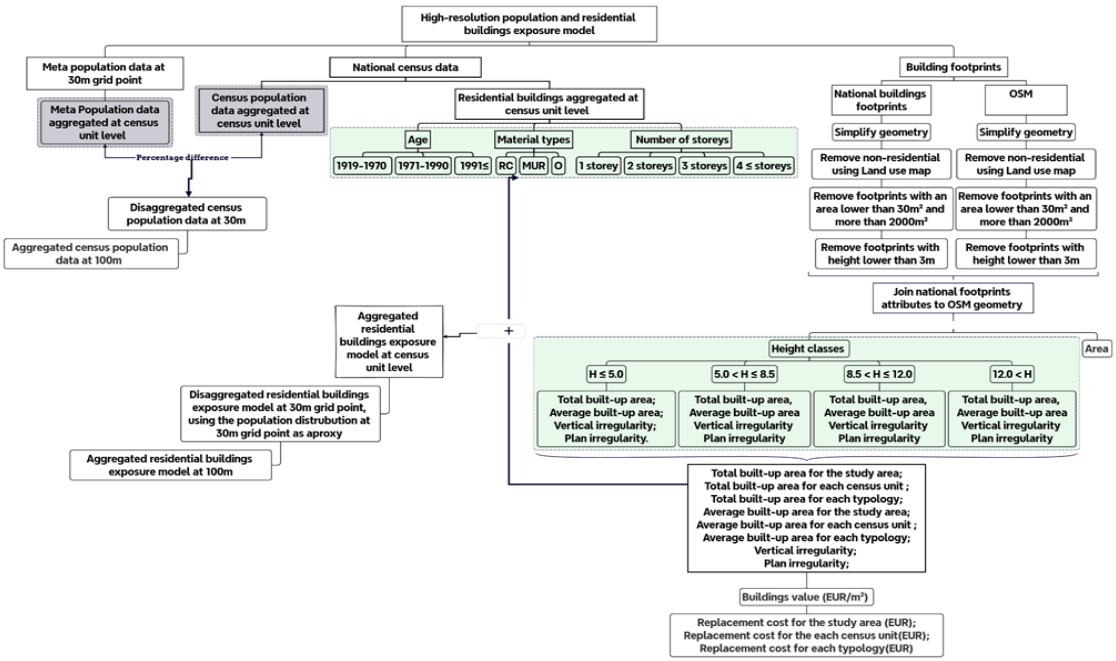

Figure 11. Flowchart illustrating the development of high-resolution population and residential buildings exposure models.

3.1.1 Datasets

National Census Data - The census data is extracted from the Italian National Institute of Statistics (ISTAT). The residential buildings data for the year 2011 (ISTAT, 2011) is used in this study, where, buildings are categorized into many typologies, based on the age (i.e. < 1919; 1919-1945; 1946-1970; 1970-1990; 1990-2005; >2005); number of storeys (i.e. 1 storey; 2 storeys; 3 storeys; 4 ≤ storeys); and construction material types (i.e. masonry; reinforced concrete; mixt from the other two types or other).

The population census data is available for 2021 from the census database (ISTAT, 2021), aggregated at the same census unit of the residential buildings. Different classes have been developed based on age (i.e. 0-5 to >74 years); gender (male, female), educational level (educated, not educated), citizenship (Italian, foreigners), number of families and employment status (employed, unemployed).

High-resolution Global Population Dataset - High-resolution Population Density Maps at a 30m pixel resolution (https://dataforgood.facebook.com/dfg/) was retrieved from Data for Good at Meta (hereinafter called Meta data for sake of easiness) for the year 2020.

Building Footprints - The digital building footprints for the study area are derived from the Carta Tecnica Regionale Numerica (CTRN, 2003) (https://eaglefvg.regione.fvg.it/) and OpenStreetMap (OSM, 2022) (https://www.openstreetmap.org/). Building footprints provide information about buildings' occupancy, area, and height which are missing in the official census data. The building footprints were also compared with the land use products in order to check their consistency.

3.1.2 Methodology

Population Exposure Layer - In the current work the high-resolution population exposure dataset is developed by combining national census data and Meta dataset. To achieve that, Meta data was aggregated to the same level as the census data. Consequently, the percentage difference between the national census and the Meta dataset is estimated. The comparison is performed for each census unit, and the percentage difference is used to correct the Meta dataset (Fig. 12) by it in each point of the Meta 30 m grid.

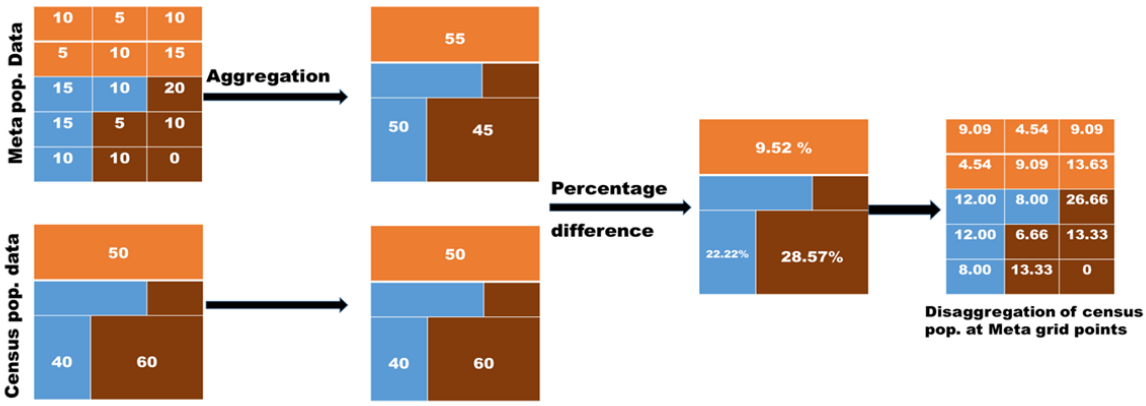

Figure 12. A flowchart of the process used to disaggregate the census population data into a 30m regular grid using the Meta population data. Each color represents a different census unit. From left to right, the flowchart shows how the meta data are aggregated at the census level resolution to compute the percentage difference, which is then applied to each cell of the high-resolution grid.

Residential Buildings Exposure Layer - The available residential buildings census data is categorized into many typologies, based on age, number of storeys and construction material types. Each census unit is characterized by several building classes, reflecting the predefined typologies of the census buildings. The residential buildings exposure dataset in the proposed methodology is assembled by combining two data sources: the last updated building census data and building footprints. The developed methodology consists of 3 steps: a) identification of height classes; b) extraction of building

characteristics from footprints; c) integration of census and footprint characteristics into a high-resolution building exposure layer (30 and 100-m) (Fig. 13). Building footprints have been used to compute average and total built-up area in each census unit and define new indicators to classify buildings based on their regularity in plan and in height. Finally, the residential buildings reconstruction cost is also computed in each census unit.

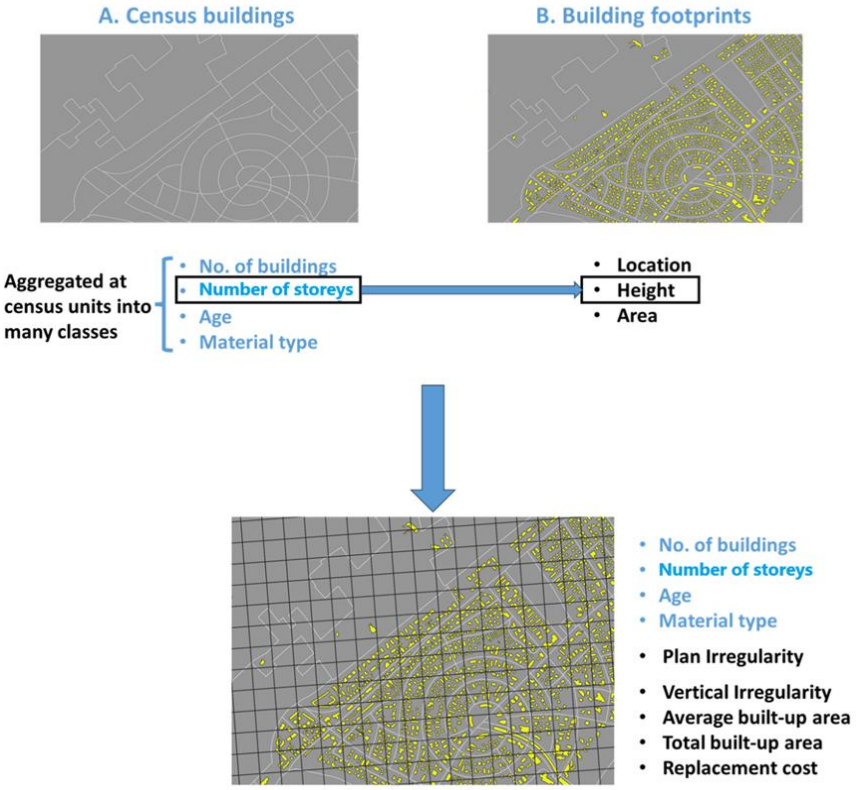

Figure 13. The procedure for generating the high-resolution building exposure layer by integrating building footprints and census data.

3.1.3 Results

The developed population exposure layers are provided at 30m and 100m resolutions (Fig. 14). Population is classified based on its demographic characteristics (i.e. population grouped into many age classes, gender distribution, night and day occupancy and number of families) and socio-economic indicators (e.g. number of citizens, foreigners, employed individuals). The developed residential building layer contains information about building age, number of storeys, construction material types, average built area, total built area, replacement cost, vertical regularity, and plan regularity, classified following the GAD4ALL taxonomy and that defined within the Return project (deliverable DV 5.2.1). The final residential building exposure layer is provided at three different resolution levels: census unit, 30m and 100m resolutions (Fig. 15). The replacement cost exposure layer is produced at the census unit level.

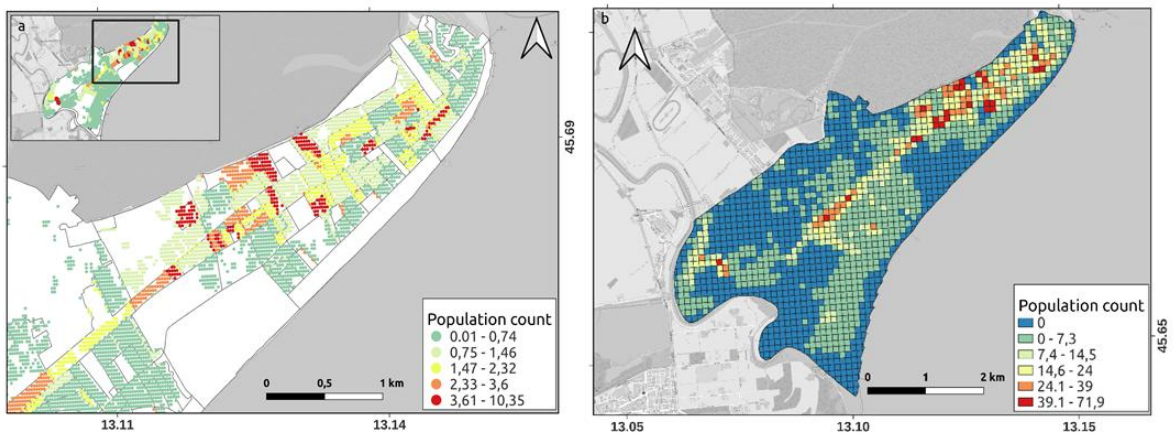

Figure 14. Exposure layers produced for population (ISTAT, 2021), a) disaggregated on a regular 30 m grid and (b) aggregated on a 100 m regular grid.

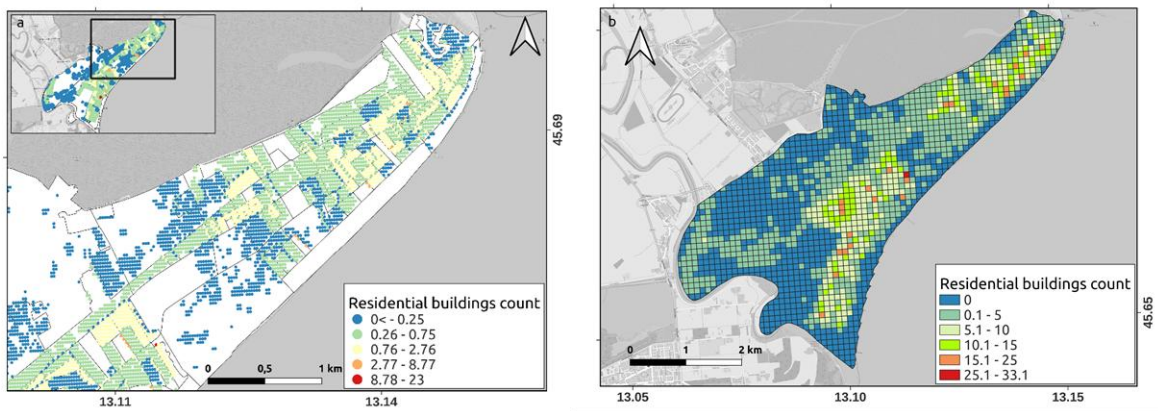

Figure 15. Exposure layers produced for residential buildings, disaggregated on a regular 30 m grid (a) and aggregated on a 100 m regular grid (b).

3.2 Identifying the risks arising from the building envelope vulnerability to several hazards

3.2.1 Introduction to the impacts of vulnerable technical elements

Buildings are composed of several elements, each designed to meet user needs, comply with legal requirements, and ensure specific performance levels over time. The building envelope is a particularly important component, tasked with providing safety, comfort, and maintainability. However, envelope elements are inherently vulnerable, as they are prone to damage due to environmental forces to which they are continuously exposed. Their degradation is inevitable and accelerated by ordinary events such as wind, solar exposure and rain, or by exceptional ones like earthquakes. This degradation process not only compromises the envelope's performance but also creates safety issues, especially in urban areas where detached facade elements may fall onto public spaces. In historic city centres, this risk is

magnified due to high pedestrian density and the aged condition of many buildings. In this sense, the elements of the building envelope become an additional hazard factor for urban systems, shifting from being elements at risk to becoming risk factors themselves.

Within this background, the Building Risk has been defined as the probability that a hazardous event, resulting from the vulnerability of the elements of the building envelope, can cause harmful effects on urban systems (Castelluccio et al., 2025a). The need for formalizing such a risk arises from the recognition that not only it is important to analyze the effects of hazardous events on the building but also to consider the impacts that the building itself may have on the surrounding context.

Assessing the consequences of damaged envelope elements is not thoroughly explored by the existing literature, even though it represents the primary concern for Public Administration in ensuring public safety. The relevance of such topic is demonstrated by the number of safety interventions performed on building envelopes by the Italian Fire Safety and Rescue Service. The authors (Castelluccio et al., 2025b) have found out that the most frequently damaged building elements pertain to the envelope. These elements are, indeed, very fragile (i.e., they very likely collapse if subject to external forces) and deteriorate with ease, the more aggressive the environment the faster the deterioration. Data reveals that the majority of the safety interventions were performed on plasters (28%), roofs (including roof coverings) (17%), and roof cornices (12%), but also windows (2%) and chimneys (2%). This means that the emergency interventions performed on building envelope's elements represent 61% of the safety interventions. Figure 16, part A, shows the interventions performed on the envelope's elements outlined with red columns. Regarding the detailed causes of intervention, the poor physical condition of the elements (34%) together with meteorological hazards (18%) and earthquakes (15%) are responsible for 67% of interventions (Fig. 16, part B).

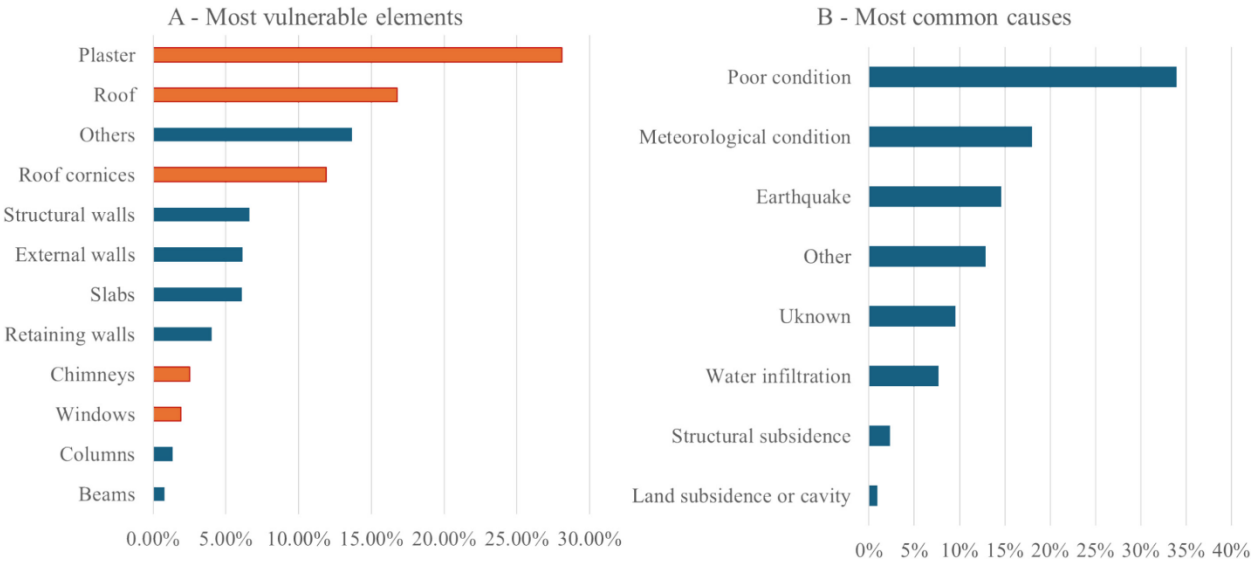

Figure 16. A – Frequency of interventions per technical element; red columns indicate interventions performed on the building envelope, and blue columns on other elements. B – Frequency of interventions by cause (source: Castelluccio et al., 2025b).

Moreover, the authors analysed how interventions are distributed across Italy. Data reveals that most interventions are performed in the South and Islands (43%), followed by Central Italy (36%) and North

(21%). Poor condition is the most frequent cause of intervention in the South (50%), earthquakes are the most frequent cause in Central Italy (37%) and adverse meteorological condition is the most frequent cause of intervention in the North (33%) (Fig. 17).

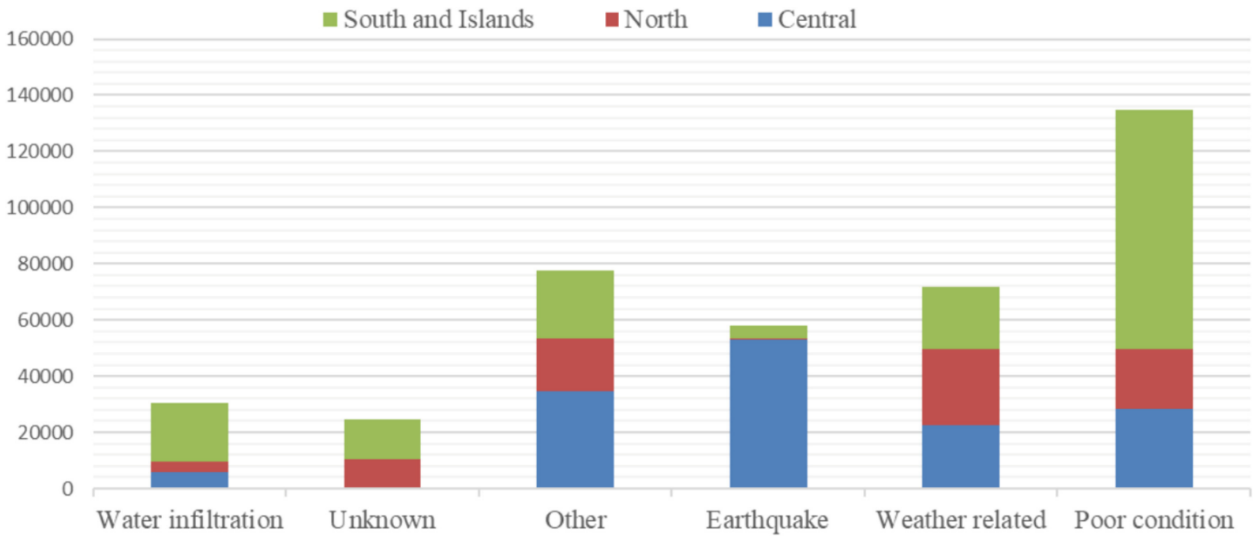

Figure 17. Frequency of interventions by geographic area and detailed cause of intervention (source: Castelluccio et al., 2025b).

The identification of the most vulnerable building elements and the most frequent cause of failure allowed the authors to develop a vulnerability assessment approach. The vulnerability assessment is required to properly evaluate the risks posed by the building itself on the surroundings, as better explained in the next section. Indeed, the more vulnerable the envelope, the greater the analysed risks (e.g., potential injuries to people due to the damaged building envelope, and road obstruction, especially escape routes).

Preliminary results on how to assess the vulnerability of building envelopes to a set of natural hazards of interest have been reported in other deliverables, i.e., DV 5.3.2 and DV 5.3.3. Also, the consequences of damaged building envelopes have been included within the existing Storylines (DV 5.3.1) and are aligned with the identified impacts (physical building damage) and related risks, i.e., physical loss of buildings' elements; injuries and fatalities; loss of productive systems; socio-economic damages to households.

More specifically, there are at least three main categories of hazardous events triggered by damaged envelope elements: safety, functional and economic losses (FEMA E-74, 2012). Regarding life safety, it is possible to mention at least injuries and fatalities, cascading damage to other objects, and road/escape/emergency route obstruction. Assessing the risk of people being injured by falling debris is an issue not thoroughly explored yet. Two studies in this regard propose a risk index evaluation (Ruggiero et al., 2021) and the calculation of the probability of detachment (Ruiz et al., 2019), both starting from the analysis of a facade's physical condition. These studies offer interesting insight, although the results are limited to homogeneous construction solutions and do not account for different hazards nor changing environmental conditions. The issue of escape route obstruction due to falling debris from facades has been exclusively analysed for seismic events, where the vulnerability of a building to an earthquake of a certain intensity is associated with the volume of debris generated due to the event and the subsequent obstruction of roads (Bernardini et al., 2022; Santarelli et al., 2018).

Functional losses may become the result of direct damaged elements or of the consequences produced by their damage. Functional losses are strictly related to economic losses. For example, a high-tech facility may have contents that are worth many times the value of the building's elements, it must be ensured, then, that these assets are not compromised by damaged elements. Finally, costs associated with damaged elements can be very extensive. This is due to repair costs and downtime. Table 1 reports the categories and some types of hazardous events triggered by damaged elements. It is worth noticing that any type of event can be translated into monetary loss, for example, injuries can be monetised through hospital treatment costs, downtimes can be translated into hours of work lost and related costs, etc.

Table 2. Examples of hazardous events triggered by damaged envelope elements.

Category	***Type***
Safety loss	Injuries and fatalities
	Road/route obstruction
	Damage to objects
Functional loss	Downtime (e.g., due to closed commercial activity)
	Additional travel time
	Number of evacuated buildings
Economic loss	Repair cost
	Cost of downtimes
	Cost of shelters

3.2.2 Building Risk assessment formulation

Within scientific domain and normative documents, risk (R) is typically characterised as the likelihood (P) that a hazardous event (United Nations General Assembly, 2016; European commission, 2010) will generate adverse impacts (D) on populations, built environments, and infrastructure, within a specific spatial and temporal frame. This idea integrates the interaction between the hazard (H) inherent to a situation, the exposure (E) of elements to that hazard, and their vulnerability (V) (Rausand, 2011). It is often synthesised in the formula $R = H \times V \times E$, wherein the scale of potential damage (D) is determined by both V and E. As a result, precise definitions of these three components are crucial for delineating a specific risk profile.

Damage represents the outcome resulting from the realisation of a hazardous event (Stanganelli, 2003), with its extent influenced by the nature of the hazard and the degree of vulnerability and exposure of the affected elements. For instance, in seismic contexts, areas with high seismic hazard but low urban density may exhibit minimal risk, whereas urbanised zones in lower hazard areas can experience elevated risk levels. Similarly, in hydrogeological settings, the impact of floods varies based on the type of exposed systems: higher risks are associated with the presence of critical infrastructure, while agricultural zones may experience comparatively lower impacts (Stanganelli, 2003; UNDRR 2022).

Vulnerability, as widely defined in literature, refers to the propensity of an element at risk to suffer damage or degradation because of a hazardous event of a specific intensity, or due to amplifying conditions related to physical, social, economic, or environmental factors (Stanganelli, 2003).

Vulnerability may be categorised in various forms, e.g., physical, economic, social, and its evaluation depends on the nature of the hazard and the characteristics of the exposed elements. Key parameters should align with the factors that best capture susceptibility. For seismic risk, for example, structural vulnerability is assessed through metrics like fragility and the capacity to endure and respond to seismic shocks. In environmental risk assessments, material compatibility with the surrounding environment becomes critical.

Exposure is understood in two principal ways: physical exposure, concerning the quantity and value of assets that may be damaged, altered, or destroyed by a hazardous event; and functional exposure, which relates to the extent to which essential services may be impaired or interrupted (Stanganelli, 2003; European Commision, 2010).

By building upon these definitions, the vulnerability of the envelope's elements (Vet) can be therefore defined as the tendency of the elements of the building envelope to suffer damage because of external hazards. This vulnerability depends on technical features (technical solutions, construction and installation methods, materials, dimensions, etc.) and the degradation level, a factor which can amplify the effect of external stresses (Castelluccio et al., 2025a). The damage to these elements, proportional to their specific Vet, determines a hazard for the urban context. This hazard, defined as Building Hazard (Hb), is identified as the probability that the fall of an element of the building envelope, i.e., the hazardous event under analysis, may occur in a specific period, in a certain area and with a certain intensity (Castelluccio et al., 2025a). Thus, the Vet influences the probability of occurrence of the hazardous event.

The expected damage caused by the Hb is related to the safety of exposed elements and depends on both System Vulnerability (Vsyst) and System Exposure (Esyst). Vsyst can vary based on characteristics such as the type of urban fabric (including regularity, distances between buildings, open spaces, and accessibility) and the ratio of building height to roadway width (Rausand, 2011). The assessment of the Esyst might refer to the number of people living and transiting in the analysed area, providing a measure of how populated a portion of the urban fabric is. It can also be measured referring to the destination and intensity of use, the value and importance of the building typologies, the level of urbanisation, and the intensity of flow services, and its assessment depends on the effects that Hb might have on the exposed elements (Castelluccio et al., 2025a).

Within common multi-risk analysis, the Building Risk (Rb) can be seen as a cascading effect triggered by other hazards, configuring itself as an additional constant risk for urban systems since its impact persistently acts on them and threatens the safety of the exposed population. However, it can also be seen as an amplifying factor that increases, for instance, the vulnerability of an urban system exposed to exceptional events, such as earthquakes or volcanic eruption, in considering the probability of obstruction of escape routes caused by the falling debris.

In conclusion, Rb is defined as "the probability that a hazardous event, resulting from the vulnerability of the technical elements of the building envelope, can cause harmful effects on urban systems" (Castelluccio et al., 2025a). It is expressed as a function of the following parameters (Eq.1): the hazard associated with the vulnerability of the technical element, (Hb); the exposure of the components in the affected urban system, (Esyst); the vulnerability of the affected urban system, (Vsyst).

(1) Rb = Hb x Vsyst x Esyst

In terms of human life safety, a reinforced concrete balcony poses a greater hazard (Hb) as its level of degradation increases, along with its mass and height above the street. The extent of damage caused by the falling element varies depending on the characteristics of the urban system, i.e., Vsyst and Esyst values. Therefore, balconies located at greater heights in urban areas with high building density and busy streets pose a significantly higher risk compared to those at lower heights in less densely built and less crowded environments. The section below reports an illustrative application on how to assess Hb for a historic building facade, starting from the vulnerability assessment of the facade's elements and their characterisation in terms of potential impact energy. This application is limited to hazard assessment, with the analysis of urban vulnerability and exposure left for future developments.

3.2.3 Illustrative application on how to assess the hazard posed by damaged facades in terms of potential injuries

With reference to the risk of injuries and fatalities (Table 1), the hazardousness of a building facade is influenced by two main factors: the vulnerability of the facade elements to the analysed hazard, which determines the probability of detachment, and the impact energy, which depends on the mass and height of the falling debris.

The analysed technical elements comprise roof covering, balconies, roof cornices, external wall finishing, roof parapet, windows and openings, drainage system elements. First, the authors have identified the hazards of greater interest, which are weather-related, i.e., strong wind, heavy rain and solar exposure/high temperature, but also earthquakes. Then they have identified the elements inherent vulnerability to each hazard, referring to available scientific literature and technical documents, including guidelines and regulations. This way, hazard-vulnerability matrixes have been developed for each element of interest. An example of hazard-vulnerability matrix is reported in Table 2, where different solutions for roof cornices are compared in terms of vulnerability to the analysed hazards. The propensity of a roof cornice to suffer damage when subject to an external force depends on the vulnerability factors identified which are driven by the element's technical characteristics, including construction technology, materials and geometry. For example, in the case of an earthquake, masonry roof cornices were deemed to be more vulnerable than reinforced concrete cornices, which were assumed to be more vulnerable than steel cornices. The description of the element's characteristics refers to the Return taxonomy (D.V. 5.2.1), although minor modifications were needed to better describe the building envelope elements.

Table 3. Roof cornice vulnerability grades to different hazards.

Cornice construction technique	Vulnerability grade per hazard			
	Earthquake	Heavy rain	Windstorm	High temperature
Unknown	n.a.	n.a.	n.a.	n.a.
Masonry, generic	Very high	Moderate	Low	Low
Stone slab with metal cantilever	Very high	Moderate	Low	Low
Hollow clay and metal cantilever	High	Low	Low	Low
Cast-in-place Reinforced Concrete	Moderate	Low	Low	Low
Precast Reinforced Concrete	High	Low	Low	Low
Steel	Low	Moderate	Moderate	High
Polystyrene /FRP / Polyurethane	Low	Low	Very high	High
Timber	Low	Very high	High	Moderate

Apart from the technical characteristics, elements suffer damage when subject to an external force proportionally to their degradation level. The degradation level is quantified considering the severity of the observed anomalies and their extension. The severity mainly refers to the type of performance alteration caused by the anomaly, thus a very mild or absent anomaly is an aesthetic alteration of the element (such as, graffiti), a mild anomaly is a superficial alteration (such as, superficial cracking), an advanced anomaly is able to compromise the mechanical properties of the element (such as, corrosion), while a severe anomaly has already led or it is about to lead the element to collapse (e.g., detachment from support, missing parts). In the end, element vulnerability can assume several values ranging from low technical vulnerability and absence of anomalies to very high technical vulnerability combined with extensive severe degradation (you can refer to Deliverable 5.3.3 for more information).

The vulnerability of the element influences the probability of detachment, while the magnitude of damage is related to its gravitational potential energy. This energy is calculated based on the mass of the potentially detached portion and its height above the ground. The detached portion can refer either to a unit surface area, which is useful for comparing different elements in terms of potential damage, or to the observed degraded area of each element for more detailed analysis.

An illustrative application demonstrates the feasibility of the approach, showing how it can be used to identify critical zones on a building facade under several disruptive circumstances (Fig. 18). This method can provide a practical and effective means to guide preventive maintenance and risk mitigation interventions. Moreover, the outputs of the analysis can be integrated with exposure and urban vulnerability assessment frameworks to support a comprehensive evaluation of the overall risk to people. The results can also be used for certain types of impact predictions, such as creating scenarios of how the feasibility of escape routes could be affected by an extreme event (e.g. an earthquake or heavy rainfall) to improve emergency plans. Immediately after an event, they can also help to anticipate the possible impact by identifying potential areas of major damage prior to a visual inspection.

Figure 18. Example of maps to identify the areas of a façade that have the greatest impact on the surroundings if a potentially disruptive event happens, such as an earthquake, heavy rainfall, high temperature, or windstorm.

3.3 Monitoring and impact forecasting models for air pollution

The ongoing menace of air pollution presents considerable obstacles to public health and environmental sustainability, highlighting the necessity for efficient monitoring and forecasting systems. With the rapid acceleration of urbanization, cities globally are witnessing a decline in air quality, which negatively impacts the health of millions. The World Health Organisation reports that air pollution results in nearly 7 million fatalities per year, underscoring the urgent need for enhanced risk management techniques (https://www.who.int/). The importance of monitoring and forecasting models lies in their capacity to amalgamate diverse data sources and approaches to predict air quality trends and associated health effects properly. Recent studies (Baklanov and Zhang 2020) have enhanced comprehension in this field which underscores the importance of high-resolution emissions data and the contribution of satellite imagery to improving forecast accuracy (Wu et al. 2025).

The literature highlights a significant focus on health effect assessments related to air pollution. Conti et al. (2017) illustrate the effectiveness of AirQ models in predicting health outcomes, establishing significant correlations between pollution and health impacts, particularly among at-risk groups, like as children (Birdal 2024). However, a significant deficiency persists in addressing the multifaceted character of air pollutants, as several studies concentrate on individual pollutant assessments rather than the aggregate effects of multiple contaminants, thereby overlooking vital insights into public health hazards (Wu et al., 2025). The structural effects of air pollution on urban infrastructure have been examined alongside health assessments (Devi et al., 2025), which reveals a direct correlation between PM emissions and the integrity of buildings in polluted areas (Castelli et al., 2020). These findings highlight the necessity for a comprehensive strategy in air quality management that incorporates both human health and structural resilience, exposing a flaw in existing methodologies that frequently overlook the interplay between air quality and infrastructure integrity (Birdal, 2024).

Recent research presents an advanced evolution of predictive models through a multi-faceted forecasting approach that integrates economic evaluations with health impact assessments (Zhai and Chen, 2018). However, while this new modeling approach enhances the understanding of air pollution's economic costs, there remains a lack of comprehensive studies addressing the entire spectrum of pollutants, thus limiting the robustness of current forecasting models. The progression of air pollution risk monitoring and impact forecasting models is evidenced by numerous significant research that underscore both advancements and ongoing concerns. Early models primarily emphasized empirical approaches, which were constrained in their ability to reliably forecast health consequences associated with air pollution, as highlighted in seminal studies that faced challenges with unprecedented emission scenarios (Ryan and Wild, 2021). With the advancement of study, the incorporation of chemical transport modeling surfaced, providing a more refined comprehension of pollutant dynamics and impacts—crucial for tackling urban air quality issues (Wu et al., 2025). The transition to advanced modeling techniques was enhanced by the incorporation of high-resolution emissions data and ground measurements, as highlighted in subsequent studies, which underscored the necessity for accurate forecasts that consider the interplay between air quality and climate change (Baklanov and Zhang, 2020). The trend of employing advanced data methodologies persisted with the introduction of the Damped Discrete Grey Prediction Model, which markedly enhanced PM2.5 forecasts from limited datasets, as detailed in recent research (Yang et al 2023). Moreover, contemporary research has commenced examining the complex effects of air pollution, encompassing both direct health consequences and economic expenditures, employing methodologies such as the "willingness to pay" approach. These techniques, albeit promising, highlight the necessity for future study to investigate multi-pollutant exposures and improve collaboration among various research communities (Conti et al. 2017; Birdal 2024).

The research demonstrates a distinct progression from basic monitoring frameworks to sophisticated, integrated models that offer actionable insights for air quality management and public health protection, indicating substantial advancement in the field (Devi et al., 2025; Yang et al., 2023). Nonetheless, the difficulties of precisely depicting dynamic pollution scenarios and guaranteeing efficient data assimilation persist as pivotal domains for future investigation. The solitary risk monitoring and impact forecasting models of air pollution demonstrate a complicated interaction of approaches and results that are essential for comprehending and regulating air quality. The significance of precise modeling is central to this discourse (Baklanov and Zhang, 2020) who assert that the amalgamation of high-resolution emissions data and sophisticated forecasting methodologies is essential for effective air quality management (Wu et al., 2025). These modeling breakthroughs facilitate public health protections and connect air quality with climate change, requiring a holistic strategy. Research emphasises the essential requirement for accurate air quality monitoring to assess health effects (Conti et al. 2017), especially concerning pollutants such as PM10 and PM2.5, which are common in urban environments and are significantly associated with severe health hazards (Conti et al., 2017). Moreover, elevated levels of particulate matter pose a public health risk and also lead to infrastructure degradation, with structural evaluations of buildings indicating substantial effects from air pollution exposure (Devi et al. 2025). Additionally, a novel forecasting system created for Beijing demonstrates a unique method for statistically analyzing the economic consequences of air pollution, highlighting the dual requirement for health impact assessments and economic evaluations (Huang, 2024). This

comprehensive perspective necessitates improved regulation of pollutants and a regional emphasis in air quality management, integrating data from multiple studies to suggest robust remedies.

The examined literature demonstrates that integrated frameworks and models can yield substantial insights into air quality management, successfully connecting health outcomes and economic costs across many contexts. The investigation of individual risk monitoring and impact forecasting models for air pollution uncovers a variety of methodological approaches that substantially affect the discipline. Empirical models prevail; yet, their dependence on statistical studies may constrain their effectiveness, especially given erratic emission patterns. Traditional empirical and statistical methods frequently falter in forecasting air quality fluctuations during extraordinary events, highlighting the necessity for more resilient predictive frameworks (Baklanov and Zhang, 2020). Conversely, chemical transport models (CTMs) are widely acknowledged for their comprehensive integration of emissions data, meteorological circumstances, and chemical reactions, facilitating a more thorough understanding of air pollution dynamics (Ryan and Wild, 2021). Recent advancements have integrated machine learning methodologies to improve predictive precision, demonstrating potential in analysing intricate datasets that conventional modelling could neglect (Wu et al., 2025). Moreover, findings from integrated assessments emphasize the necessity of addressing dynamic urban landscapes, where diverse pollution sources require customised strategies (Birdal, 2024). It is necessary to have a comprehensive methodological transition towards systems thinking, promoting models that predict pollution levels while also evaluating health and economic consequences, exemplified by the Damped Discrete Grey Prediction Model introduced in recent literature, which enhances accuracy with constrained data (Yang et al 2023). Furthermore, techniques that integrate health assessments with economic evaluations offer essential insights into the wider ramifications of pollution, aiding in successful policy formulation (Conti et al., 2017). As academics increasingly advocate for interdisciplinary collaboration, the necessity of updating existing models becomes evident, particularly to simultaneously address various pollutants and enhance risk assessments (Huang, 2024). The continual methodological advancement ensures a thorough comprehension of air pollution's impacts, highlighting the need for innovation in monitoring and forecasting methods. The examination of theoretical frameworks in individual risk assessment and impact prediction models of air pollution demonstrates considerable interaction among several paradigms. Conventional empirical models have frequently been contested by the intricate dynamics of air quality; for instance, research underscores the insufficiency of empirical/statistical methods to effectively forecast impacts in unprecedented emission scenarios, thereby requiring more sophisticated chemical transport models (Ryan and Wild, 2021). This transition highlights the increasing acknowledgement of integrated methodologies that combine predictive modelling with health effect assessments, emphasizing the need for accurate air quality monitoring to forecast health outcomes, especially for vulnerable populations (Conti et al., 2017). This aligns with findings that stress the significance of frameworks that consider multiple pollutants rather than isolated analyses (Wu et al. 2025). Moreover, Baklanov and Zhang (2020) substantiates this claim by illustrating the intricate interconnections between pollutants and health concerns, which bear significance for policy and regulation. Theoretical breakthroughs like the Damped Discrete Grey Prediction Model (FDGM(1,1)) provide unique ways for forecasting PM2.5 with enhanced accuracy; yet literature highlights difficulties surrounding the singular emphasis on particulate matter. This prompts essential inquiries about the thoroughness of current models, compelling researchers to broaden their analytical framework to

encompass various pollutants (Yang et al., 2023). Furthermore, interdisciplinary collaboration, as shown in numerous studies, is essential for enhancing air quality forecasting and developing efficient public health measures (Birdal, 2024). Ultimately, the literature indicates that reconciling theoretical disparities among diverse modelling methodologies fosters a thorough comprehension of air pollution dynamics, underscoring the necessity for ongoing enhancement and amalgamation of multiple theoretical frameworks to tackle urban air quality issues (Devi et al., 2025; Huang, 2024).

In conclusion, the results highlight the intricacy of precisely forecasting air quality and its related health consequences, particularly due to the complicated interactions among diverse contaminants and their effects on public health and urban infrastructure. Consequently, there is an imperative need for additional research to investigate the interconnections among diverse contaminants and to create integrated models that can guide health effect assessments and economic evaluations within a unified framework. The ramifications for policy and practice are significant, since the incorporation of advanced models can enhance decision-making and policy measures designed to mitigate air pollution exposure. This can ultimately enhance public health outcomes and promote environmental sustainability. Moreover, interdisciplinary collaboration among researchers from many domains is crucial to enhance existing approaches and foster innovations that address the difficulties of air quality management. Subsequent studies must emphasize the improvement of data assimilation methodologies, utilize machine learning for the analysis of intricate datasets, and broaden the analytical scope to incorporate comprehensive models that consider the cumulative impacts of many pollutants (Huang, 2024). The continuous advancement of air pollution monitoring and forecasting models is a critical domain for additional investigation and funding. By addressing the identified deficiencies in the literature and pursuing a more integrative methodology, researchers might enhance the creation of resilient urban landscapes equipped to confront critical challenges related to air quality and public health. The importance of this initiative is paramount, as effective air quality management is essential for protecting public health and the environment in the context of rising urbanization and climate change.

3.4 Integrated assessment of health-connected risks from air pollution with a special focus on emerging pollutants

The catastrophic London smog of 1952, which killed an estimated 12 000 people, prompted governments to monitor and regulate air pollution. Early legislation focused on coarse soot and sulphur dioxide because these were visible, measurable, and obviously linked to coal combustion. Fast forward to the twenty first century: emissions shifted from coal to oil and gas; vehicles replaced hearths as the primary urban source; and scientists armed with satellites, micro sensors, and omics technologies began to uncover a hidden layer of danger. Fine particles smaller than a human hair—and gases we cannot smell—penetrate deep into our lungs, enter the bloodstream, and travel to organs never before implicated in “smog” deaths, including the brain and placenta. Today, curbside monitors in megacities routinely record BC peaks of 15 $\mu g\, m^{-3}$, NO_2 spikes above 150 $\mu g\, m^{-3}$, and UFP counts that top 150 000 particles cm^{-3} during the morning commute (EEA 2024; EUROPE BC 2024). These pollutants originate from common combustion processes -diesel engines, biomass stoves, industrial furnaces- yet their atmospheric behavior and biological impacts diverge. The challenge for scientists and policymakers is therefore two-fold. First, we must understand how simultaneous exposure to BC, NOx, and UFP affects the human body throughout the life course, from in utero development to late life

neurodegeneration. Second, we must craft interventions that avoid the pitfall of single pollutant tunnel vision; a policy that suppresses BC by banning diesel buses but raises UFP from tire wear, for instance, may yield unexpected tradeoffs. In this chapter, we promote an integrated lens that captures these interconnections, with a deliberate emphasis on equity: who breathes the dirtiest air, and who benefits first when pollution falls?

3.4.1 Conceptual Framework for Integrated Risk Assessment

Integrated Risk Assessment (IRA) adapts the classical four-step paradigm -hazard identification, exposure assessment, dose-response estimation, and risk characterization- to the reality that humans inhale mixtures rather than isolated pollutants

Hazard identification

The first step catalogues the relevant agents and their toxicological properties. Black carbon's potency derives from its large surface area and ability to adsorb carcinogenic polycyclic aromatic hydrocarbons; NO_2 is a powerful oxidant that provokes airway inflammation; UFP owe their toxicity to nanoscale size, enabling them to cross epithelial and even placental barriers. By comparing toxicological endpoints (oxidative stress markers, cytotoxicity assays, DNA-methylation profiles) researchers now rank these pollutants not just by concentration but by oxidative potential (OP) and reactive oxygen species (ROS) generation capability.

Exposure assessment

Traditional fixed-site monitors offer hourly or daily averages but miss alley-way hotspots and personal micro-environments. Recent advances include satellite instruments such as TROPOMI-TROPOspheric Monitoring Instrument (NO_2 columns) and MAIA-Multi-Angle Imager for Aerosols (BC and PM composition); low-cost optical and electrochemical sensors deployed in dense citizen-science networks; and wearable devices that log an individual's inhaled dose each minute. Machine-learning land-use regression (LUR) models integrate these data sources, achieving spatial resolutions below 100 m and mean-bias errors of < 1 µg m^{-3} for BC or <5 µg m^{-3} for NO_2.

Dose-response estimation.

While early epidemiological studies assumed linear relationships, modern analyses employ flexible splines that capture steep risk increases at low concentrations, then plateau effects. The Global Exposure Mortality Model for BC (GEMM-BC 2025), for instance, pooled 24 cohorts and found an accelerated hazard ratio at concentrations below 1 µg m^{-3}, suggesting no safe threshold. For NO_2, time-series studies reveal near-instant cardiovascular responses, whereas UFP exhibit both acute cardiopulmonary triggers and chronic neurodegenerative links.

Risk characterization and integration.

The final step combines pollutant-specific dose-response functions with population vulnerability linked to age, comorbidities, socio-economic status, to estimate Disability-Adjusted Life Years (DALYs) and monetize damages via the Value of Statistical Life (VSL). Tools such as BenMAP-CE and WHO's AirQ+ can now ingest BC, NO_2, and UFP simultaneously, outputting city-level or neighborhood-level burden

estimates. Crucially, these platforms allow scenario analysis: planners can test whether banning diesel in a low-emission zone (LEZ) delivers more DALYs averted than subsidizing heat-pump replacements for biomass stoves, and at what cost.

3.4.2 Black Carbon (BC)

Sources and spatio-temporal patterns

In high-income cities, diesel vehicles account for up to 60 % of urban BC emissions, with construction machinery and residential wood-burning following behind. In lower-income regions, the picture flips: traditional cookstoves, brick kilns, and open waste burning dominate.

Italy provides a revealing European case study. The densely populated Po Valley, stretching from Turin through Milan to Venice, combines heavy diesel traffic, an expansive logistics sector, and widespread wintertime wood-stove use. Persistent thermal inversions trap pollutants beneath a low mixing height, allowing BC to accumulate for days. Annual-mean BC measured by the regional environment agencies (ARPA) reaches 2–3 $\mu g\ m^{-3}$ at urban-background sites in Milan and Turin and spikes to 6–8 $\mu g\ m^{-3}$ at curbside monitors during morning rush hour. Source-apportionment campaigns attribute roughly 45 % of urban BC to traffic, 30 % to domestic wood-burning, and the remainder to industry and agricultural burning. The Italian National Institute of Health (ISS 2025) estimates that BC contributes to about 9 000 premature deaths each year nationwide, with Lombardy and Veneto bearing nearly half of the burden. Satellite retrievals using the Multi-Angle Imager for Aerosols (MAIA) highlight the Po Valley as one of Europe's three persistent BC hot-spots, rivalled only by the Upper Silesian coal basin and Germany's Ruhr region.

Exposure and Measurement

Most regulatory networks measure $PM_{2.5}$ mass but not BC specifically, leaving a surveillance gap. Aethalometers (e.g., AE33) and multi-angle absorption photometers (MAAP) provide real-time optical estimates of BC and can distinguish fossil-fuel from biomass signatures via wavelength-dependent absorption. More advanced single-particle incandescence instruments (SP2) quantify refractory BC mass of individual soot particles, offering insights into mixing state, but remain expensive and laboratory-oriented. For community monitoring, portable micro-aethalometers (AE51) and emerging LED-photoacoustic sensors cost a few hundred euros and, after calibration, track reference instruments within ±15 %, as demonstrated in the Breathe-London pilot, which revealed local plumes five times above background outside bus depots. Instrument choice follows purpose: regulatory trends rely on filter-based EC for comparability; alert systems favor optical instruments for second-level resolution; and research campaigns deploy SP2 for detailed morphology. Even today, the current legislation does not clearly define the methods of evaluating this pollutant, nor the limit concentrations for the population at risk.

Toxicology and Epidemiology

At the molecular level, BC acts as a Trojan horse, ferrying metals like iron, copper, and manganese into alveolar macrophages, catalyzing the Fenton reaction and generating hydroxyl radicals. In vitro assays show BC induces mitochondrial DNA damage and nuclear factor-κB (NF-κB) activation, driving pro-inflammatory cytokine release. In animal models, short-term BC exposure triggers endothelial

dysfunction within 24 hours, reducing flow-mediated dilation. Human evidence is equally compelling: a meta-analysis of 24 cohorts covering 8 million participants found an 11 % increase in all-cause mortality per 1 µg m^{-3} long-term BC exposure (GEMM-BC 2025). Children are particularly vulnerable; the ongoing HELIX birth cohort reports that prenatal BC exposure lowers full-scale IQ by 2.3 points per 0.5 µg m^{-3} and increases the risk of attention-deficit/hyperactivity disorder.

3.4.3 Nitrogen Oxides (NOx)

Atmospheric Chemistry in a Nutshell

Nitric oxide (NO) forms during high-temperature combustion; within minutes it oxidizes to nitrogen dioxide (NO_2). Sunlight photolysis NO_2 back to NO, liberating atomic oxygen that combines with O_2 to form ozone (O_3). NOx thus sits at the nexus of ozone and secondary aerosol production: cutting NOx can suppress both O_3 and nitrate PM. Despite selective catalytic reduction (SCR) in power plants, real-world NOx emissions from vehicles remain stubbornly high. Euro 6-certified diesel cars, for example, emit up to 2 times the laboratory limit in winter because SCR catalysts underperform at low exhaust temperatures.

Exposure Pathways

Chemiluminescence analyzers anchor national networks with hourly NO_2 data, yet monitors are sparse in low-income neighborhoods. Passive diffusion tubes, costing €30 each, fill spatial gaps and reveal curb-to-alley gradients exceeding 300 %. Indoors, gas stoves without ventilation hoods can spike NO_2 to 150 µg m^{-3} (triple the WHO daily guideline) underscoring that outdoor regulation alone cannot guarantee safe indoor air. Personal monitoring in the Barcelona NOx-Kids study found that children in classrooms without mechanical ventilation were exposed to daily averages 20 µg m^{-3} higher than those in ventilated schools.

Health Evidence and Mechanisms

Once inhaled, NO_2 diffuses into airway surface fluid, where it forms nitrite and nitric acid, lowering pH and oxidizing epithelial membranes. This damage triggers release of interleukins that amplify allergic sensitization. A 2023 HEI meta-analysis (HEI Panel on NO_2 2023) concluded that prenatal NO_2 raises childhood-asthma odds by 26 % per 10 µg m^{-3}. Cardiovascular impacts are increasingly evident: a pooled time-series across 20 European cities found a 0.8 % increase in daily stroke admissions per 10 µg m^{-3} NO_2 rise (GEMM-NO_2 2024). Emerging studies also link chronic NO_2 exposure to insulin resistance and type-2 diabetes, possibly via systemic inflammation and oxidative stress.

Policies in Practice

Between 2018 and 2022, Taiwan retrofitted 37 coal- and oil-fired power-plant units with advanced selective catalytic-reduction (SCR) systems. Stack measurements show an average 85 % drop in NO_x emissions—from 320 mg Nm^{-3} to 45 mg Nm^{-3}—which coincided with a 12 % decline in respiratory-disease hospital admissions across the downwind districts of Taichung, Changhua, and Yunlin. Satellite retrievals of tropospheric NO_2 columns confirmed a regional 9 % decrease, illustrating that plant-level interventions can yield benefits far beyond the facility fence line.

At the metropolitan scale, Madrid's ambitious "Bosque Metropolitano" project—an encircling 75-km urban forest corridor comprising two million drought-tolerant trees—functions as more than a carbon sink. Computational-fluid-dynamics modelling indicates that the vegetative belt enhances mechanical turbulence and dry deposition, shaving annual-mean roadside NO_2 by 3 µg m^{-3} and lowering peak summertime ozone by 1 ppb in adjacent barrios. Co-benefits include a 1.5 °C reduction in land-surface temperature during heatwaves and a projected 7 % increase in pedestrian activity along newly shaded corridors.

Europe's expanding network of low-emission zones (LEZs) provide further evidence that traffic policy can deliver rapid air-quality gains before the entire vehicle fleet turns over. High-resolution curbside monitoring reveals that London's Ultra-Low Emission Zone (ULEZ) cut roadside NO_2 by 39 µg m^{-3} (-46 %) within its first 24 months (London Mayor's Office 2025), Berlin's Umweltzone achieved a 22 µg m^{-3} (-26 %) reduction, and Milan's Area C tallied a 24 µg m^{-3} (-29 %) decrease. These improvements occurred despite continued growth in passenger-kilometers travelled, underscoring the potency of stringent emissions standards, congestion fees, and robust enforcement to shift behavior and improve public health.

3.4.4 Ultrafine Particles (UFP)

Why Size Matters

Particles smaller than 100 nm have a surface-area-to-mass ratio orders of magnitude greater than coarse PM, enabling them to carry a large load of redox-active chemicals per microgram. UFP penetrate deep into alveoli, cross epithelial barriers, enter the bloodstream, and even reach the brain via olfactory nerves, bypassing the blood-brain barrier. Sources include incomplete combustion, brake and tire wear, and photochemical nucleation when volatile organic gases condense, especially in sunny, low-NOx conditions.

Measuring an Invisible Threat

Because UFP contribute only a few micrograms per cubic meter to ambient PM mass, they slide under the radar of gravimetric filters that underpin most regulatory standards. Capturing their abundance therefore requires instruments that count or charge every particle rather than weigh them. The work-horse is the Condensation Particle Counter (CPC), which enlarges each nano-sized particle via butanol or water vapor condensation and then detects the resulting droplets optically, producing a total-number concentration (usually expressed as particles cm^{-3}). Complementing CPCs are Scanning Mobility Particle Sizers (SMPS) and Electrical Mobility Spectrometers (DMS), which classify particles by their electrical mobility, providing high-resolution size distributions from 10 nm to 500 nm. For field campaigns where size spectra are less critical than toxicity proxies, diffusion chargers estimate the lung-deposited surface area (LDSA), arguably a more health-relevant metric than simple number counts because deposited area governs oxidative-stress potential. Pocket-sized instruments such as the DiSCmini now allow personal exposure studies, revealing subway commuters in Seoul inhaling LDSA doses three-times higher than bus riders despite similar $PM_{2.5}$ mass. At the regulatory level, the current proposal is to use only CPCs to estimate the number of UPF: the logic followed is that the total number of particles is driven by the finest ones. However, the complete study of the size distribution is the basis for understanding the processes from which UFPs originate and the consequent mitigation policies.

Spatial heterogeneity is striking in San Francisco, the Google Street View car network traversed 30 000 road segments and uncovered freeway "canyons" where UFP counts were ten-fold the city average, while sheltered residential cul-de-sacs registered background levels (Apte 2024). Fixed regulatory stations would have missed these micro-hotspots entirely. To bridge this gap, Europe's GAIA-UFP network is piloting >200 low-cost optical-diffusion sensors, each maintained with a cloud-based auto-calibration routine tied to collocated reference CPCs.

Satellite detection of UFP is still in its infancy because conventional aerosol-optical-depth products are dominated by larger particles. Nevertheless, multispectral-polarimetric payloads such as APEX and the upcoming 3MI on MetOp-SG aim to retrieve columnar UFP proxies by exploiting the strong angular dependence of Rayleigh-like scattering from sub-100 nm particles. Early validation flights over the Po Valley show a promising correlation ($R^2 \approx 0.55$) with aircraft CPC counts, but systematic ground-truth calibration is essential before policy-grade retrievals become routine. Combining these forthcoming satellite products with dense ground networks could finally deliver the multiscale exposure surfaces needed for global UFP health-burden assessment.

Health Impacts and Biology

UFP's nanoscale size facilitates cellular uptake. Once internalized, they generate reactive oxygen species, damage mitochondria, and trigger pro-inflammatory pathways. The HEI-UFP meta-analysis (2024) linked a 10 000 particles cm^{-3} increase in long-term UFP exposure to a 7 % rise in cardiovascular mortality. Prenatal exposure correlates with pre-eclampsia and low birth-weight; in older adults UFP exposure associates with faster cognitive decline and Parkinson's disease onset. Mechanistic studies show that UFP disrupt tight-junction proteins in the blood–brain barrier, potentially facilitating neuroinflammation.

Mitigation Outlook

Across Europe, a multi-tier strategy is emerging to shrink the continent's ultrafine-particle footprint.

Aviation hot-spots. Zurich airport's upgrade to fixed electric ground power and self-propelled e-tugs was the proof of concept: apron UFP concentrations fell by 50 % within two years and passenger-terminal PM_{10} limits were beaten by an additional 18 %. Amsterdam–Schiphol (Schiphol Airport Authority, 2024) has since electrified 100 % of its air-side vehicle fleet (both baggage tractors and catering trucks) delivering a 60 % curb-side UFP cut and prompting the European Union Aviation Safety Agency (EASA) to draft continent-wide "Clean Airport" guidelines.

Road transport. Beginning in 2025, Sweden and Germany will mandate low-abrasion, copper-free brake pads, a move expected to eliminate 7 000 t yr^{-1} of non-exhaust PM. Field trials in Stuttgart logged a 15 % drop in roadside UFP numbers and a 40 % reduction in brake-wear metals (Cu, Sb, Ba). Barcelona's Eixample district, meanwhile, piloted deep-clean road-dust vacuum sweepers that removed three tons of tire particulate in six months, translating into a further 9 % local UFP decrease.

Euro VII and beyond. The forthcoming Euro VII regulation (European Commission, 2025, target adoption 2027) tightens tail-pipe particle-number limits from a 23 nm to a 10 nm cut-off, capturing the vast majority of nucleation-mode particles. For the first time, it also sets a brake-particle-number cap of 7×10^{11} particles km^{-1} and a tire-abrasion mass limit of 2 mg km^{-1}. European Environment Agency

modelling suggests full implementation could shave up to 32 % off urban UFP exposure by 2035 and avert 11 000 premature deaths annually.

Urban mobility policies. More than 320 European cities now operate low- or zero-emission zones. Milan's Area C introduced a non-exhaust UFP surcharge for Euro 3/4 diesel delivery vans in 2024, spurring a 30 % surge in electric-van registrations and a measured 12 % curb-side particle-number fall within a year. London's pilot "Zero-Emission Bus Zone" on Route 7 records a 50 % reduction in UFP peaks whenever battery-electric buses replace Euro VI hybrids.

Taken together, these aviation, vehicular, and regulatory measures paint an optimistic mitigation outlook: if enforcement parallels ambition, Europe could realize a 20–35 % decline in urban UFP exposure over the next decade—while simultaneously slashing noise, greenhouse gases, and roadside metal pollution.

3.4.5 Cross-Cutting Themes

Environmental Justice

Air-pollution exposure is not evenly distributed. As an example, in Los Angeles census tracts with the highest NO_2 also rank in the top decile for UFP; 80 % of their residents are Hispanic or Black (USC 2024). Nairobi's slums endure double the BC of affluent neighborhoods. Such inequalities mean that cleaner air is not merely a technical challenge but a moral imperative. Analyses using the Gini coefficient show that, while overall pollution has declined in many cities, inequality in exposure has remained stubbornly high.

Synergistic Toxicity

Because pollutants rarely act in isolation, researchers are turning to Bayesian kernel-machine regression and quantile-based g-computation to model mixture effects. A US emergency-room study found a supra-additive interaction between BC and NO_2 on asthma visits. In vitro, co-exposure to UFP and NO_2 amplifies oxidative DNA damage beyond the sum of individual exposures. These findings argue for multipollutant standards rather than pollutant-by-pollutant limits.

Indoor–Outdoor Coupling

Indoor air quality is shaped by infiltration of outdoor pollutants and by indoor sources like gas stoves, candles, and 3D printers. A hybrid infiltration model finds that naturally ventilated homes admit 65 % of outdoor UFP versus 25 % in mechanically ventilated offices. Gas stoves can triple indoor NO_2 concentrations, illustrating the need to align ambient-air regulation with building codes and appliance standards.

3.4.6 Methodological Advances

Advances in monitoring hardware, data science, and economic modelling have transformed the way researchers quantify and value air-pollution risks. This section expands on those developments and spells out every acronym at first use so that the reader encounters no unexplained shorthand.

Sensors and satellite innovation

- **MAIA – Multi-Angle Imager for Aerosols** (NASA–ASI, launched 2024) combines multi-angle, multi-spectral, and multi-polarization observations to retrieve black-carbon (BC) and organic-carbon columns at 1 km resolution. By pairing these satellite data with ground monitors, city planners in Los Angeles and Milan are generating high-fidelity exposure maps for epidemiological studies.

- **WHO-AQ-Hub – World Health Organization Air-Quality Hub** streams real-time data from 12 000 low-cost sensors (electrochemical for NO_2, optical for BC, diffusion-charger for ultrafine particles – UFP) into a publicly accessible dashboard. Open-access Application Programming Interfaces (APIs) allow researchers to pull minute-level data for rapid-response health analyses after wildfire smoke events.

- **APEX – Airborne Prism EXperiment** is a hyperspectral imaging spectrometer flown on small aircraft; it resolves 5 m ground pixels and can infer UFP proxies by exploiting the angular scattering signature of sub-100 nm particles. Although currently a research platform, APEX has been pivotal in validating the forthcoming 3MI – Multi-Viewing, Multi-Channel, Multi-Polarization Imaging instrument on Europe's MetOp-SG satellite.

- For surface monitoring, next-generation **CPCs – Condensation Particle Counters and SMPS – Scanning Mobility Particle Sizers** now ship with auto-calibration modules and Bluetooth connectivity, enabling long-term autonomous deployment. Compact diffusion-charger units estimate LDSA – Lung-Deposited Surface Area, a toxicity-weighted metric increasingly adopted in health studies.

Analytics

- **TMLE – Targeted Maximum-Likelihood Estimation and BKMR – Bayesian Kernel Machine Regression** have become the work-horses for estimating non-linear, multi-pollutant dose–response functions while controlling for high-dimensional confounding. In the 65-million-person US Medicare cohort, TMLE separated BC and NO_2 mortality risks without the variance inflation common to traditional two-pollutant models.

- **BCF – Bayesian Causal Forests and Granger-causal networks** are being trained on fused environmental and electronic-health-record (EHR) data to detect early-warning pollution signatures for asthma exacerbations.

- **Federated learning (FL)** frameworks keep personal health data on local hospital servers while sharing encrypted model parameters—circumventing privacy barriers that once hampered multi-centre studies.

Economics

- **SCC – Social Cost of Carbon** values have been expanded to include BC's short-lived climate forcing: the GAINS – Greenhouse-gas and Air-pollution Interactions and Synergies model now prices BC at € 110 t^{-1} CO_2-eq. This monetization allows direct comparison between climate and health co-benefits in cost-effectiveness analyses.

- The **BenMAP-CE – Environmental Benefits Mapping and Analysis Program–Community Edition** integrates pollutant-specific dose-response functions for BC, NO_2, and UFP, enabling city planners to tabulate avoided deaths, hospitalizations, and lost-work days under competing mitigation scenarios.

- **CBAs – Cost-Benefit Analyses** increasingly adopt VSL – Value of a Statistical Life adjustments that scale with local income, ensuring that benefit estimates in lower- and middle-income countries are not undervalued.

Collectively, these methodological advances close critical gaps—from detecting nanometer-scale particles to valuing their societal impacts, thus empowering policymakers with sharper, faster, and fairer tools for integrated air-quality management.

3.4.7 Policy Roadmap

The route to cleaner, healthier air can be visualized as a ladder with three interlocking rungs—each adding depth rather than substituting for the others.

Rung 1 — Source-specific controls (2025 and sooner). These surgical interventions tackle the heaviest emitters first. Mandatory diesel-particulate-filter (DPF) retrofits for buses and refuse trucks, rapid deployment of selective catalytic-reduction burners in power stations and cement kilns and recall programs for Euro 5/6 diesel cars that exceed real-driving emissions can slash curb-side black-carbon (BC) and nitrogen-oxide (NOx) peaks within a single inspection cycle. In the non-exhaust realm, copper-free, low-abrasion brake pads are poised to trim roadside ultrafine-particle (UFP) counts by 10–20 %. Because the requisite technologies already exist and plug into familiar maintenance workflows, payback is swift: London's diesel-bus retrofits, for instance, offset their capital cost via reduced hospital admissions in just 18 months.

Rung 2 — Systemic shifts (2025 – 2040). Once the low-hanging fruit is harvested, deeper structural change yields multiplicative benefits. Electrifying urban bus fleets and last-mile delivery vans removes tail-pipe NOx and BC while paving the way for quieter streets and lower maintenance bills. The gains are magnified when the electricity grid itself decarbonizes and district-heat pumps replace gas boilers, preventing up-wind emission displacement. A European Commission meta-analysis finds that achieving a 60 % electric-vehicle share supplied by an 80 % renewable grid would drive down urban UFP exposure by 25 % and CO_2 emissions by 50 % relative to 2020 baselines.

Rung 3 — Behavioral and equity measures (ongoing). Technology alone cannot erase the exposure gap; demand-side and community-centered policies are essential. Congestion charging in Stockholm and Milan has cut vehicle-kilometers travelled by 15–20 % and sliced peak NO_2 by up to 30 %. Fare-free or low-fare public-transport passes for low-income households ensure that cleaner air does not come at the cost of mobility. Meanwhile, citizen-science sensor networks (such as Barcelona's Xair and London's Breathe sensors) arm residents with hyper-local evidence to lobby for traffic-calming, tree planting, and clean-school-street initiatives.

Taken together, the three rungs form a coherent climb. **Integrated-assessment modelling** shows that completing all stages could avert 3 million premature deaths and 0.4 °C of global warming by 2050 (UNEP-CCAC 2022), with more than half of the health benefits accruing to communities currently in the highest exposure decile.

3.4.8 Research Gaps and Future Directions

- **Harmonizing UFP Metrics**: Current proposals differ on whether to regulate particles < 10 nm or < 23 nm. Toxicology suggests the smaller cut-off, but measurement remains challenging.
- **Non-Tailpipe BC**: As engines clean up, brake- and tire-derived soot may dominate urban BC by 2035, yet emission factors are poorly characterized.
- **Climate Feedback**: BC deposition on snow affects monsoon dynamics and agricultural yields—an area ripe for Earth-system modelling.
- **Synergistic Exposures**: Heat waves co-occurring with BC-NO_2-UFP mixtures may push vulnerable populations beyond physiological tipping points; coupled climate health models are needed

3.4.9 Conclusions

Air pollution control is at a crossroads. The technologies to curb BC, NOx, and UFP exist (diesel filters, electrified transport, clean cooking) but their deployment is uneven. Adopting an integrated, equity-centered perspective can maximize health gains, slow climate change, and narrow exposure disparities within a generation. Policymakers must act decisively, guided by robust science and empowered communities.

3.5 A detailed 3D geological model of the Florence basin for the estimation earthquake scenarios

Earthquakes are among the most dangerous and unpredictable natural hazards. Their impact can be severe and long-lasting, affecting not only human lives but also the socio-economic fabric of entire communities. History has shown that major earthquakes often leave consequences that extend far beyond their immediate effects, altering the historical trajectory of populations and regions.

Today, the effects of earthquakes are particularly dramatic in urban areas, where population density is highest and exposure is amplified by the concentration and vulnerability of buildings and infrastructure. For this reason, earthquakes have long been the focus of extensive scientific research. Decades of progress in seismology have significantly advanced our understanding of seismic processes, enabling more accurate risk assessments, improved preventive strategies, and more effective planning for seismic retrofitting.

Looking ahead, enhancing our understanding of seismic risk will require integrating innovative technologies—such as remote sensing, powerful software, and numerical modeling—with traditional field-based observations, which remain essential for studying geological hazards. This integrated approach forms the foundation of the present work.

3.5.1 Earthquake physics and seismic wave propagation

Earthquakes result from the sudden release of elastic energy that has accumulated over decades along a fault zone. Most of this energy is dissipated as heat along the fault surface, while a smaller portion is radiated as seismic waves that travel through the Earth and reach the surface. The intensity of an earthquake felt at a given location is influenced by several factors, including:

• the characteristics of the seismic source and rupture propagation;

• the propagation of seismic waves;

• site effects.

Numerous studies have shown that the impact of an earthquake can vary significantly depending on the geological and geomorphological features of the area. Consequently, even within a small region, the same earthquake can be felt—and recorded—differently due to variations in subsurface geology. This phenomenon, known as seismic amplification, is primarily caused by lithostratigraphic conditions and typically occurs in specific geological settings such as sedimentary basins, where loosely consolidated soft sediments overlie a bedrock composed of compacted, cemented rocks. The contact between these domains, which have different mechanical properties, creates a strong impedance contrast that alters the characteristics of the incident seismic waves (Pitarka and Irikura, 1998; Lee et al., 2008). This impedance contrast can occur even in areas with relatively small-scale variations in both spatial extent and subsurface thickness, depending on local geological conditions.

Seismic wave amplification within sedimentary basins is also influenced by topographic conditions. In such cases, relief along the basin margins can focus seismic waves, and the reflection of these waves at the free surface can interact with incoming waves, potentially resulting in significant amplification effects. A well-known example of site effects is the 1985 Michoacán earthquake in Mexico. The shaking experienced in Mexico City—located about 400 kilometers from the epicenter—varied dramatically across the urban area. These effects were not only observed but also measured: seismic stations located close to one another recorded markedly different seismograms. Since the distance from the source was essentially the same for all stations, the differences in ground motion can be attributed solely to variations in near-surface geology (Mayoral et al., 2019).

3.5.2 Site amplification challenges and subsurface modeling

The causes of seismic amplification are difficult to evaluate, as they depend on highly localized geological variations. For example, in terms of lithological site effects, more competent layers within the poorly consolidated Quaternary cover sediments can act as impedance contrast levels similar to the primary bedrock–sediment interface. Therefore, it is crucial not only to identify the presence of such layers but also to understand their extention along the basin. Knowing the geometry and distribution of impedance contrast surfaces between different lithologies is of primary importance.

One of the main tools currently used to address site effects is seismic microzonation (https://rischi.protezionecivile.gov.it/it/sismico/attivita/microzonazione-sismica/). This process involves dividing a territory based on how the ground is expected to respond to a seismic event and is mandatory for all urbanized areas in Italy. Although different levels of study and detail are considered based on the area's complexity, the resulting acceleration parameters—while extremely important—are derived from point measurements. These do not fully account for the three-dimensional distribution of lithotypes or the dynamic behavior of seismic waves in space. Therefore, reconstructing the stratigraphic layering of the subsurface, identifying the different lithotypes, and assessing their mechanical and physical properties is critically important. For this reason, high-resolution 3D geological modeling is the first step toward a proper evaluation of the seismic risk in a given area.

The goal of this work is to reconstruct the 3D subsurface geology of a specific area—identified within the Florence–Prato–Pistoia basin—using modeling software. This will provide a basis for future numerical simulations aimed at estimating 3D seismic wave propagation and evaluating amplification phenomena.

3.5.3 Study area: The Geological and seismotectonic settings of the Florence-Prato-Pistoia Basin

The Florence–Prato–Pistoia Basin (hereafter referred to as the Florence Basin) is a tectonic basin located in northern Tuscany (Italy), within the geographic transition zone between the Northern Apennines and the Tuscan Chianti Hills. The basin is traversed by the Arno River, which flows from east to west and serves as the main hydrological axis. Over time, the Arno has incised into the basin's sedimentary fill, creating a narrow floodplain and associated fluvial terraces. The present-day landscape reflects the combined effects of tectonic subsidence, alluvial sedimentation, and subsequent fluvial erosion.

The Florence Basin is a NW–SE trending geomorphological depression, whose formation is associated with post-orogenic extensional processes that have affected the area from the Neogene to the Quaternary (Carmignani et al., 2001). Consistent with its tectonic origin, the basin is bounded by normal faults that have played a key role in its subsidence, creating accommodation space for sediment accumulation. The recent activity of some of these faults, such as the Fiesole Fault, remains under debate.

The bedrock of the Florence Basin consists of the Ligurian Unit and the Tuscan Nappe succession, whose complex structural relationships are observable along the mountain ridges surrounding the basin.

The Plio-Pleistocene successions that infill the basin unconformably overlie this Meso-Cenozoic bedrock. These recent deposits, characterized by poorly consolidated rocks, are composed mainly of alternating sands and clay-rich sediments. The stratigraphic sequences (Synthems) clearly document the transition from lacustrine to fluvial depositional environments.

In the metropolitan area of Florence, the cover deposits mainly consist of bluish-grey lacustrine silty clays, interbedded with gravelly and sandy fan deposits from tributary streams. These sediments thicken toward the northeast near the Fiesole Fault, reaching approximately 120 meters, and thin toward the southwest due to bedrock uplift and erosion. The upper layers transition into organic-rich silts and paleosols, indicating a shift toward marshy, limno-palustrine conditions.

The thickness of the Quaternary deposits increases significantly toward the northwest, reaching up to 500 meters (Capecchi et al., 1975).

The sedimentary fill of the Florence Basin exhibits marked variability both longitudinally and transversely, as highlighted by field surveys and geotechnical investigations. Additionally, the sediments originate from diverse depositional environments, resulting in significant heterogeneity in their mechanical properties. Combined with the highly irregular bedrock morphology and the wedge-shaped narrowing of the valley near Florence, these factors contribute to conditions that may enhance seismic amplification within the basin.

Although the Florence Basin is characterized by moderate seismicity, historical records report several impactful earthquakes. The 1542 Mugello event (Mw ≈ 6.0) reached intensity VIII MCS. On 18 May 1895, a Mw ≈ 5.4 quake caused intensity VIII MCS near the epicenter and VII MCS in Florence. The 1919

Mugello earthquake (Mw 6.3, intensity X MCS) resulted in over 100 fatalities and widespread destruction in Vicchio and nearby towns. Although its epicenter lay northeast of the basin, it was strongly felt in Florence, highlighting how even distant quakes can significantly affect the area due to its complex geology and dense urbanization (Montabert et al., 2020; Bonini et al., 2022).

3.5.4 3D Geological Model

A 3D geological model of the subsurface beneath the urban area of Florence was developed using a combination of modeling software, including Leapfrog® Geo, and GIS tools (Fig. 19). The primary objective of the model is to reconstruct the thickness and three-dimensional architecture of the various Quaternary lithotypes, as well as the geometry of the main bedrock interface—defined by the contact between the more competent lithologies of the Tuscan Nappe and Liguride Units, and the overlying, less consolidated Quaternary deposits.

The reconstruction was based on the integration of multiple datasets:

- A 10×10 m digital elevation model (DEM), provided by Regione Toscana, which defines the upper boundary of the model. Key features such as well locations were plotted onto this surface.
- Borehole data, comprising over 2,000 stratigraphic logs from various sources, including the Tuscan Regional Administration and the Municipality of Florence.
- Gravimetric data provided by ENI, under an agreement with ISPRA for the compilation of CARG Sheet 275.

Borehole data were organized within a dedicated three-dimensional geognostic database, specifically designed to support 3D geological modeling.

This comprehensive dataset enabled the identification and classification of distinct synthems, each corresponding to specific depositional environments, further confirmed through field observations. Additionally, the geometry of the bedrock surface was accurately interpreted from borehole data and successfully reconstructed in three dimensions. The resulting model offers a high-resolution framework for understanding the subsurface architecture of the Florence Basin.

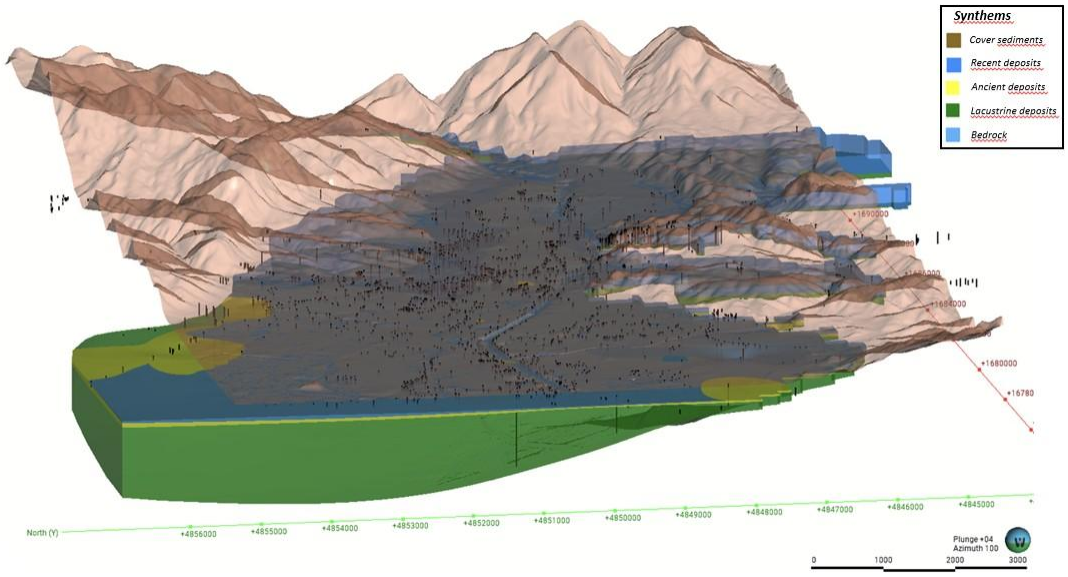

Figure 19. 3D geological model of the Florence area.

3.5.5 Remarks

The preliminary results of this study offer valuable insights into the geological and structural configuration of the subsurface in the Florence area. In particular, the 3D geological model provides rapid and detailed information on key subsurface features, such as structural heterogeneities (e.g., buried fault scarps) and the thickness, distribution, and stratification of Quaternary cover deposits.

These geological characteristics can significantly influence the propagation and amplification of seismic waves, especially in structurally complex basins like Florence. Understanding these subsurface dynamics is therefore fundamental for seismic risk mitigation.

This knowledge provides a crucial foundation for the development of future physics-based numerical models, which aim to simulate ground motion scenarios with greater accuracy. Such models will support not only hazard assessments but also urban planning and civil protection strategies, particularly in areas where local site conditions are known to exacerbate seismic shaking. The integration of geological modeling with seismic response analysis represents a forward-looking approach to improving seismic resilience in densely urbanized regions.

References

Abadie, L.M., Galarraga, I., Markandya, A., de Murieta, E.S. 2019. “Risk measures and the distribution of damage curves for 600 European coastal cities.” *Environ. Res. Lett.* 14: 064021. https://doi.org/10.1088/1748-9326/ab185c

Abadie, L.M., Sainz de Murieta, E., Galarraga, I. 2016. “Climate risk assessment under uncertainty: An application to main European coastal cities.” *Front. Mar. Sci.* 3: 265. https://doi.org/10.3389/fmars.2016.00265

Achebak, H., Garatachea, R., Pay, M.T. et al. 2024. "Geographic sources of ozone air pollution and mortality burden in Europe." *Nat Med* 30: 1732–1738. https://doi.org/10.1038/s41591-024-02976-x

Adamek K, Vasan N, Elshaer A, English E, Bitsuamlak G. (2017). Pedestrian level wind assessment through city development: a study of the financial district in Toronto. *Sustain. Cities Soc.* 35: 178-190.

Afzal S, Riaz RA, Kim BS (2016). "Energy-efficient flood detection and evacuation system using WSN technology." *IEEE Access* 4: 3285-3296.

Ahmed I, Esch M, Hoeven F (2023). Heatwave vulnerability across different spatial scales: Insights from the Dutch built environment. *Urban Climate* 51: 101614.

APEX Team (2023). Airborne Prism EXperiment: Instrument overview and data applications. *Remote Sensing of Environment*.

Baklanov A, Zhang Y (2020). Advances in air quality modeling and forecasting. *Global Transitions* 2:261-270. https://doi.org/10.1016/j.glt.2020.11.001.

Basili R, Brizuela B, Herrero A, Iqbal S, et al. (2019). *NEAMTHM18 documentation: The making of the TSUMAPSNEAM tsunami hazard model 2018*. Istituto Nazionale di Geofisica e Vulcanologia (INGV). https://doi.org/10.5281/zenodo.3406625.

Bernardini G, Ferreira TM (2022). Combining structural and non-structural risk-reduction measures to improve evacuation safety in historical built environments. *International Journal of Architectural Heritage* 16:820–838. https://doi.org/10.1080/15583058.2021.2001117

Birdal RG (2024). Air pollution impact on forecasting electricity demand utilizing CNN-PSO hyper-parameter optimization. *Environ. Res. Commun*. 6:055022. https://doi.org/10.1088/2515-7620/ad484b

Bonini L, Sani F, Montone P, Antonioli A, et al. (2022). Recent seismic sequences and activation of normal fault systems in the Mugello Basin and surrounding areas (Northern Apennines, Italy). *Tectonics* 41:e2021TC006946. https://doi.org/10.1029/2021TC006946

Bragato PL, Boaga J, Capotosti G, et al. (2025). Implementing a dense accelerometer network in Veneto (NE Italy): a support for rapid earthquake impact assessment. *Bulletin of Earthquake Engineering* 23:1859–1884. https://doi.org/10.1007/s10518-025-02133-w

Calderón-Garcidueñas L, et al. (2024). Black carbon nanoparticles in the human brain. *Environmental Research*.

CanCHEC-NO_2 Study Group (2022). Chronic nitrogen dioxide exposure and COPD in Canadian cohorts. Am. J. Respir. Crit. Care Med.

Capecchi F, Guazzone G, Pranzini G (1975). Il bacino lacustre di Firenze-Prato-Pistoia; geologia del sottosuolo e ricostruzione evolutiva. *Italian Journal of Geosciences* 94:637–660.

Carmignani L, Decandia FA, Disperati L, et al. (2001). Tectonic framework of the Northern Apennines and Western Alps. *Episodes* 24:171–175. https://doi.org/10.18814/epiiugs/2001/v24i3/002

Carta Tecnica Regionale Numerica CTRN (2003). Eaglefvg - Sistema di consultazione delle banche dati territoriali della Regione Autonoma Friuli Venezia Giulia. https://eaglefvg.regione.fvg.it/ (last access 7 July 2024).

Caruso A, Colombelli S, Elia L, Picozzi M, Zollo A (2017). An on-site alert level early warning system for Italy. *J. Geophys. Res. Solid Earth* 122:2106-2118. https://doi.org/10.1002/2016JB013403.

Castelli M, Clemente FM, Popovič A, Silva S, Vanneschi L (2020). A Machine Learning Approach to Predict Air Quality in California. *Complexity* 2020:8049504. https://doi.org/10.1155/2020/8049504

Castelluccio R, Fraiese M, Vitiello V (2025a). Identifying building risk: The potential consequences of the vulnerability of building envelopes' technical elements. *TeMa*. https://doi.org/10.30682/tema110002

Castelluccio R, Marmo R, Vitiello V, Ponticell L (2025b). *Most vulnerable building technical elements in a multi-hazard scenario*. In Mazzolani FM, Landolfo R, Faggiano B (Eds.), Protection of Historical Constructions. PROHITECH 2025. Lecture Notes in Civil Engineering (Vol. 595). Springer, Cham. https://doi.org/10.1007/978-3-031-87312-6_16

Conti GO, Heibati B, Kloog I, et al (2017). A review of AirQ Models and their applications for forecasting the air pollution health outcomes. *Environ. Sci. Pollut. Res.* 24:6426–6445. https://doi.org/10.1007/s11356-016-8180-1

Devi LP, Chandana R, Bandhu D (2025). Assessment and forecasting of particulate matter emissions and structural health monitoring of buildings in Bangalore. *Sci. Rep.* 15:17805. https://doi.org/10.1038/s41598-025-00814-9

DISS Working Group (2021). *Database of Individual Seismogenic Sources (DISS), Version 3.3.0: A compilation of potential sources for earthquakes larger than M 5.5 in Italy and surrounding areas*. Istituto Nazionale di Geofisica e Vulcanologia (INGV). https://doi.org/10.13127/diss3.3.0

EASA – European Union Aviation Safety Agency (2024). *Clean Airport Guidelines*. Cologne: EASA.

EEA – European Environment Agency (2024). Air Quality in Europe 2024 Report. Copenhagen: EEA.

European Commission. (2010). *Risk assessment and mapping guidelines for disaster management*. Commission Staff Working Paper, Brussels, Belgium. Retrieved September 4, 2024, from https://ec.europa.eu/echo/files/about/COMM_PDF_SEC_2010_1626_F_staff_working_document_en.pdf

European Commission (2025). *Euro VII Regulation Proposal for Light- and Heavy-Duty Vehicles*. Brussels: EC.

Facebook Connectivity Lab and Center for International Earth Science Information Network – CIESIN – Columbia University (2024). *Uzebekistan: High Resolution Population Density Maps + Demographic Estimates, Humanitarian Data Exchange (HDX) repository* [dataset], https://data.humdata.org/dataset/uzbekistan-high-resolution-population-density-maps-demographic-estimates (last access: 7 July 2024).

Federal Emergency Management Agency (FEMA) (2012). *E-74: Reducing the risks of non-structural earthquake damage—a practical guide*. Washington, DC.

Figueiredo R, Martina M (2016). Using open building data in the development of exposure data sets for catastrophe risk modelling. *Natural Hazards and Earth System Sciences* 16:417-429. https://doi.org/10.5194/nhess-16-417-2016.

GAIA-UFP Consortium (2025). Low-cost sensor network for ultrafine particle monitoring across Europe. *Atmospheric Measurement Techniques*.

GAINS-Europe Model Team (2024). *Health and climate co-benefits of black carbon and methane mitigation in Europe*. IIASA, Laxenburg.

GEMM-BC Study Group (2025). Global exposure mortality model for black carbon. *Environmental Health Perspectives*.

GEMM-NO_2 Consortium (2024). Short-term nitrogen dioxide exposure and stroke admissions across Europe. *Environmental Epidemiology*.

HEI Panel on NO_2 (2023). *Review of the evidence on health effects of nitrogen dioxide*. Boston: Health Effects Institute.

HEI-UFP Research Committee (2024). *Ultrafine particles: Systematic review and meta-analysis of cardiovascular mortality.* J. Am. Heart Assoc.

Huang Q (2024) Theoretical basis and analytical framework for the impact of air pollution on the labor supply of middle-aged and elderly people in rural areas. *International Journal of Frontiers in Sociology* 6:18-27 https://dx.doi.org/10.25236/IJFS.2024.060904

ISTAT (2011). *15° Censimento della popolazione e delle abitazioni 2011, National buildings census*. Istituto Nazionale di Statistica, Rome,Italy (in Italian).

ISTAT (2021). *Censimento della popolazione e delle abitazioni 2021, National buildings census*. Istituto Nazionale di Statistica, Rome,Italy (in Italian).

Lee J, Heaton TH, Hall JF (2008). Effects of realistic topography on seismic-wave propagation: A numerical study in the Taipei Basin, Taiwan. *Bulletin of the Seismological Society of America* 98:1685–1695. https://doi.org/10.1785/0120070200

London Mayor's Office (2025). *Ultra Low Emission Zone (ULEZ) health-impact evaluation report*. London: GLA.

Mayoral JC, Valencia VA, Soto R (2019). Site effects on seismic wave amplification in Mexico City: An analysis of the 1985 Michoacán earthquake. *Soil Dynamics and Earthquake Engineering* 119:210–221. https://doi.org/10.1016/j.soildyn.2018.12.010

Medicare-BC Cohort (2024). Black carbon exposure and cognitive decline among US seniors. *J. Am. Geriatr. Soc*.

Montabert C, Leucci G, Negri S, Leoni G, Mazzoli S (2020). Tracing the seismic history of Sant'Agata del Mugello (Italy, Tuscany) through a cross-disciplinary approach. *Natural Hazards* 104:727–749. https://doi.org/10.1007/s11069-020-04179-6

OpenStreetMap – OSM (2022). https://www.openstreetmap.org/#map=13/45.67109/13.12265/ (last access 28 February 2025).

Peresan A, Hassan HM (2024). Scenario-based tsunami hazard assessment for Northeastern Adriatic coasts. *Med. Geosc. Rev.* 6:87-110. https://doi.org/10.1007/s42990-024-00114-w

Petrovic B, Scaini C, Parolai S (2023) The damage assessment for rapid response (DARR) method and its application to different ground-motion levels and Building types. *Seismol. Res. Lett*. 94:1536-1555. https://doi.org/10.1785/0220210350

Pitarka A, Irikura K. (1998). Amplification of seismic waves in sedimentary basins: Numerical simulations for realistic 3D basin models. *Bulletin of the Seismological Society of America* 88:1453–1463. https://doi.org/10.1785/0120170067

Poggi V, Scaini C, Moratto L, Peressi G, Comelli P, Bragato PL, Parolai S (2021) Rapid damage scenario assessment for earthquake emergency management. *Seismol Res Lett* 92:2513–2530. https://doi.org/10.1785/0220200245

Rausand M (2011). *Risk assessment: Theory, methods, and applications (1st ed.).* Hoboken, New Jersey: John Wiley & Sons.

Ruiz F, Aguado A, Serrat C, Casas JR (2019). Condition assessment of building façades based on hazard to people*. Structure and Infrastructure Engineering* 15:1346–1365. https://doi.org/10.1080/15732479.2019.1621907

Ruggiero G, Marmo R, Nicolella MA (2021). Methodological approach for assessing the safety of historic buildings' façades. *Sustainability* 13:2812. https://doi.org/10.3390/su13052812

Ryan E, Wild O (2021). Calibrating a global atmospheric chemistry transport model using Gaussian process emulation and ground-level concentrations of ozone and carbon monoxide. *Geosci. Model Dev.* 14:5373–5391. https://doi.org/10.5194/gmd-14-5373-2021

Santarelli S, Bernardini G, Quagliarini E, D'Orazio M (2018). New indices for the existing city-centers streets network reliability and availability assessment in earthquake emergency*. International Journal of Architectural Heritage* 12:153–168. https://doi.org/10.1080/15583058.2017.1328543

Schiphol Airport Authority (2024). *Electrified taxiing and apron UFP reduction at Amsterdam-Schiphol*. Aviation Environment Federation Bulletin.

Stanganelli M (2003). *Prevenzione e mitigazione dei rischi naturali nella pianificazione urbana e territoriale*. Napoli: Giannini.

Tocchi G, Polese M, Di Ludovico M, Prota A (2022) Regional based exposure models to account for local building typologies. *Bulletin of Earthquake Engineering* 20:193-228. https://doi.org/10.1007/s10518-021-01242-6

Tunini L, Zuliani D, Di Traglia F et al. (2024). Monitoring and modelling moraine landslides: an example from Cazzaso village (Carnic Alps, Italy). *Bulletin of Geophysics and Oceanography* 65:327-346. https://doi.org/10.4430/bgo00459

United Nations General Assembly (2016). *Report of the open-ended intergovernmental expert working group on indicators and terminology relating to disaster risk reduction*. Geneva, Switzerland. Retrieved January 21, 2024, from https://www.preventionweb.net/quick/11605

UNDRR. (2022). *Technical guidance on comprehensive risk assessment and planning in the context of climate change*. Geneva, Switzerland. Retrieved January 26, 2024, from https://www.undrr.org/quick/71077

UNEP-CCAC – United Nations Environment Programme & Climate and Clean Air Coalition (2022). *Integration of black carbon, methane, and nitrogen-oxide mitigation for climate and health benefits*. Paris: CCAC.

USC Environmental Justice Map Team (2024). *Multi-pollutant exposure disparities across Los Angeles County*. Environmental Justice.

Wells DL, Coppersmith KJ (1994). New Empirical Relationships among Magnitude, Rupture Length, Rupture Width, Rupture Area, and Surface Displacement. *Bulletin of the Seismological Society of America* 84:974–1002. https://doi.org/10.1785/BSSA0840040974

WHO – World Health Organization (2024). *Ambient (outdoor) air pollution fact sheet № 9*. Geneva: WHO.

WHO-AQ-Hub Team (2025). *Global deployment of WHO Air-Quality Hub sensors: Technical summary*. Geneva: WHO.

Worden CB, Thompson EM, Hearne M, Wald DJ (2020). *ShakeMap Manual Online: technical manual, user's guide, and software guide*. U. S. Geological Survey. https://doi.org/10.5066/F7D21VPQ

Wu C, Wang R, Lu S, Tian J, Yin L, Wang L, Zheng W (2025). Time-Series Data-Driven PM2.5 Forecasting: From Theoretical Framework to Empirical Analysis. *Atmosphere* 16:292. https://doi.org/10.3390/atmos16030292

Xhafaj E, Hassan HM, Scaini C, Peresan A (2024). Simulation of large plausible tsunami scenarios associated with the 2019 Durres (Albania) earthquake source and adjacent seismogenic zones. *Med. Geosc. Rev.* 6:197–217. https://doi.org/10.1007/s42990-024-00122-w

Yalciner AC, Pelinovsky E, Zaytsev A, Kurkin A, Ozer C, Karakus H (2006). *NamiDance manual*. Middle East Technical University Civil Engineering Department, Ocean Engineering Research Center, Ankara.

Yang W, Wang J, Zhang K., Hao Y (2023) A novel air pollution forecasting, health effects, and economic cost assessment system for environmental management: From a new perspective of the district-level. *Journal of Cleaner Production* 417:138027. https://doi.org/10.1016/j.jclepro.2023.138027

Zaytsev A, Yalciner A, Chernov A, Pelinovsky E (2019). *Tsunami Numerical Model Nami Dance GPU User Manual*. METU - Middle East Technical University. Retrieved January 17, 2021, from https://www.metu.edu.tr/

Zhai B, Chen J (2018) Development of a stacked ensemble model for forecasting and analyzing daily average PM2.5 concentrations in Beijing, China. *Science of The Total Environment* 635:644-658. https://doi.org/10.1016/j.scitotenv.2018.04.040.

Zuliani D, Tunini L, Di Traglia F, Chersich M, Curone D (2022). Cost-Effective, Single-Frequency GPS Network as a Tool for Landslide Monitoring. *Sensors* 22:3526. https://doi.org/10.3390/s22093526

Zurich Airport Authority (2023). Airside electrification programme: Impact on ultrafine particle exposure. *Airport Environment Quarterly*.